Influence of the synthesis parameters on the proton exchange membrane fuel cells performance of Fe–N–C aerogel catalysts

Youling Wang, Mikkel J Larsen, Sergio Rojas, Moulay Tahar Sougrati, Frederic Jaouen, Pilar Ferrer, Diego Gianolio, Sandrine Berthon-Fabry

▶ **To cite this version:**

Youling Wang, Mikkel J Larsen, Sergio Rojas, Moulay Tahar Sougrati, Frederic Jaouen, et al.. Influence of the synthesis parameters on the proton exchange membrane fuel cells performance of Fe–N–C aerogel catalysts. Journal of Power Sources, 2021, 514, pp.230561. ⟨10.1016/j.jpowsour.2021.230561⟩. ⟨hal-03361259⟩

HAL Id: hal-03361259

https://hal.science/hal-03361259v1

Submitted on 5 Oct 2021

HAL is a multi-disciplinary open access archive for the deposit and dissemination of scientific research documents, whether they are published or not. The documents may come from teaching and research institutions in France or abroad, or from public or private research centers.

L'archive ouverte pluridisciplinaire **HAL**, est destinée au dépôt et à la diffusion de documents scientifiques de niveau recherche, publiés ou non, émanant des établissements d'enseignement et de recherche français ou étrangers, des laboratoires publics ou privés.

HAL Authorization

Influence of the synthesis parameters on the Proton Exchange Membrane Fuel Cells performance of Fe-N-C aerogel catalysts

Youling Wang [a], Mikkel J. Larsen [b], Sergio Rojas [c], Moulay-Tahar Sougrati,[d] Frédéric Jaouen [d], Pilar Ferrer[e], Diego Gianolio[e], Sandrine Berthon-Fabry [a,*]

[a] MINES ParisTech, PSL University, Centre procédés, énergies renouvelables et systèmes énergétiques (PERSEE) CS 10207 rue Claude Daunesse, 06904, Sophia Antipolis Cedex, France

[b] IRD Fuel Cells A/S, Emil Neckelmanns Vej 15 A&B, DK-5220 Odense SØ, Denmark

[c] Grupo de Energía y Química Sostenibles, Instituto de Catálisia s y Petroleoquímca, CSIC, Marie Curie 2, 28049, Madrid, Spain

[d] ICGM, Univ. Montpellier, CNRS, ENSCM, Montpellier, France

[e]Diamond Light Source, Harwell Science and Innovation Campus, Didcot, OX11 0DE, UK

*Corresponding author.

E-mail address: sandrine.berthon-fabry@mines-paristech.fr (S. Berthon-Fabry). Tel: +33 493957547

Abstract

Fe-N-C aerogel catalysts were prepared by sol–gel polycondensation of resorcinol, melamine and formaldehyde precursors in the presence of $FeCl_3$ salt, followed by supercritical drying and thermal treatments. The effect of the mass ratio of precursors on the microstructure, iron speciation and oxygen reduction reaction (ORR) performance of the Fe-N-C aerogels was investigated by N_2 sorption, scanning electron microscopy, X-ray diffraction, X-ray photoelectron spectroscopy, Mössbauer spectroscopy, X-ray absorption spectroscopy, CO chemisorption and rotating disk electrode in acidic medium. The best ORR performance (activity and mass transport) was obtained by an optimum balance between pore structure and active Fe-N_x species. Through acid washing, the

durability of the catalyst was further improved by eliminating unstable and inactive species, particularly iron nanoparticles and iron carbide. From the CO chemisorption and turnover-frequency value, the surface sites were comparable with the highest values reported in literature. Finally, Fe-N-C aerogel catalyst was implemented a in membrane–electrode assembly with an active area of 25 cm^2 and tested in single cell, emphasizing the importance of the ink formulation on the performance.

Key words: Non-precious metal catalyst, carbon aerogel, acidic media, oxygen reduction reaction, PEMFCs

Graphical abstract

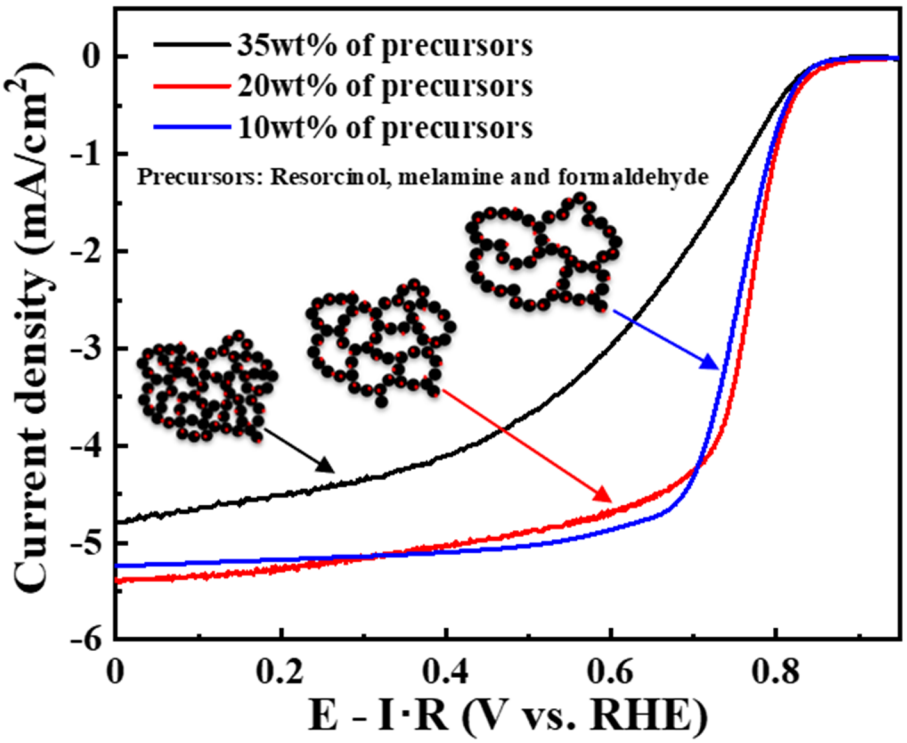

Highlights

- Optimum balance between pore texture and active FeNx species for best ORR performance
- Better mass-transport properties due to higher mesopore volume in the Fe-N-C catalyst
- XAS and ^{57}Fe Mössbauer spectroscopies identified FeN_x and Fe-inorganic species.
- Acid washing treatment eliminates the unstable and inactive Fe-inorganic species
- Need to adapt the ink formulation to the catalyst texture for high performance MEAs

1 Introduction

Owing to their advantages including high energy efficiency, scalability and environmental friendliness, proton exchange membrane fuel cells (PEMFCs) have been regarded as one of the most attractive energy technologies to respond to the increasing energy demand and the environmental deterioration. So far, Pt-based catalysts are commonly used on both anode and cathode. Moreover, the sluggish kinetics of the oxygen reduction reaction (ORR), even on Pt surfaces, requires a high Pt loading on the cathode to reach sufficient power density [1, 2]. The resulting high Pt loading in the PEMFC stacks increases the overall cost of the system, hindering their commercialisation. To decrease the raw materials' cost of PEMFC stacks and increase their environmental sustainability, numerous efforts have been made to develop non-precious metal cathode catalysts (NPMCs) in order to replace Pt-based catalysts [2-6]. Among various NPMCs, Fe-N-C catalysts have been regarded as the most promising alternative hitherto, and tremendous progress has been made in terms of catalytic activity and stability in the last decade [2, 3, 7-9]. From the vast amount of literature on Fe-N-C catalysts reported in the last 10 years, several important consensuses have been reached. First, atomically-dispersed Fe-N_4 sites are now commonly accepted to be the most active and selective centres in complex Fe-N-C materials for the 4-electron ORR process in acidic medium [10-12]. Second, the porosity characteristics of catalysts is another significant attribute determining the catalytic performance. A proper pore size distribution for Fe-N-C catalysts is essential because micro-pores host the Fe-N_4 while mesopores and macropores are responsible for the mass transport properties of the catalyst layer [12, 13]. To obtain an optimal pore structure with high specific surface area and a balanced combination of micro- and meso-pores, various approaches have been employed such as using template (e.g. sacrificial support, salt template) and incorporating other inactive species (SiO_2) during the synthesis of Fe-N-C catalysts [14-18]. Atanassov et al. employed silica in their hard-template approach. Fe-N-C catalysts with high surface area and a 3D porous structure could be

obtained after etching the template by hydrofluoric acid [14-17]. However, this introduces multiple post-pyrolysis leaching steps, and raises also environmental issues, and cost issues in scaling-up such a synthesis approach. Yang et al. employed SiO_2 nanoparticle chains to modify the mesoporous structure and wettability of Fe-N-C catalysts [18]. Compared with the reference Fe-N-C catalyst, the SiO_2-Fe-N-C catalyst exhibited similar intrinsic activity but better mass-transport properties according to the H_2/air PEMFC polarisation curves. Due to their 3D porous structure, high surface area and controllable pore size distribution, carbon aerogels (CAs) appear to be another promising path for preparing Fe-N-C ORR catalysts. The pore structure of CAs could be effectively preserved via supercritical drying technique, and highly porous structure could be obtained without incorporating any inactive species (e.g. SiO_2) or using any template and avoiding the subsequent procedure for template removal. Moreover, the morphology, texture and composition of CAs can be easily adjusted by simply varying the parameters of the synthesis, such as the sol's pH, reaction temperature, the nature of C-precursors and the polycondensation catalyst used, their relative contents, etc. On the other hand, heteroatoms (e.g. N, S) and non-precious metals (e.g. Fe, Co) could be easily incorporated into the carbon matrix of CA [19] [20], which could improve the basicity and wettability of the resulting carbon surface, beneficial for the promotion of electron transfer reactions. However, so far, the ORR catalytic activities of the reported aerogel-derived catalysts in acid media are relatively low compared with those of Fe-N-C catalysts derived from metal organic frameworks, and in particular from zeolitic imidazolate frameworks (ZIF) [6, 10, 12, 21-23]. Researches on three-dimensional covalent organic framework porphyrin aerogels are carried out by Elbaz team in order to combine the advantages of both systems [24].

Herein, Fe-N-C aerogel catalysts were firstly prepared by a sol-gel polymerization of resorcinol, melamine, formaldehyde with $FeCl_3$, followed by supercritical drying and heat-treatments in N_2 and NH_3 atmosphere. This work leans on the results from our previous work, where we studied

the effect of chemical and process parameters on the microstructure, composition and ORR performance [19]. In order to further improve the catalytic activity for the ORR, the optimization of the synthesis condition was carried out by adjusting the reactant to solvent ratio and heat-treatment protocol. Their effect on the physicochemical properties (structure, texture property and chemical composition) and electrochemical performance for the ORR were studied. The relation between the physicochemical properties and ORR performance are discussed and several structure-performance correlations could be established. Through acid washing removing unstable and poorly-active Fe species, the durability of the optimized catalyst was further improved. Furthermore, the structure of the active sites within the optimized Fe-N-C aerogel catalysts has been identified with ^{57}Fe Mössbauer spectroscopy and X-ray absorption spectroscopy (XAS), and the site density quantified by using cryogenic CO chemisorption. Finally, the effect of the ink formulation on the performance of the Fe-N-C aerogel catalyst in a PEMFC cathode was studied in single cell. It has been found that not only the catalyst characteristics affect the performance, but also the composition of the ink to set up the catalytic layer in the membrane–electrode assembly (MEA) must be designed according to the texture and chemical surface state of the catalyst to achieve the best performance.

2 Experimental

2.1 Sample synthesis

The Fe containing hydrogels were prepared by a modified pre-polycondensation procedure using resorcinol (R, 99%, Alfa Aesar), melamine (M, 99%, Acros Organics), formaldehyde (F, 37 wt% solution, Acros Organics) and iron chloride ($FeCl_3$, anhydrous, pure, Acros Organics) as precursors, sodium carbonate (C, Na_2CO_3 anhydrous, 99.9999%, Fluka) as polycondensation catalyst and deionized water as solvent (S) [19, 25]. The precursors and the catalyst were mixed with water under stirring at 70°C for 40 min with the molar ratio of 2:7:1:0.033 for R:F:M:C. From this, aqueous solutions containing different cumulative mass fractions of the reactants were prepared by varying

the quantity of deionized water added. Solutions with a cumulative R, M and F mass fraction of 35, 20 or 10% were prepared. $FeCl_3$ was then added to the solution, with a fixed Fe/R molar ratio of 0.015 in all cases. Then, NaOH solution of 2 mol L^{-1} was used to adjust the pH of the sol to 8 and the sol was stirred at 70°C until gelation. Subsequently, the gel was kept in water bath for 120 h at 70 °C as the aging process of the polymerized gel. Then, the hydrogels were subjected to water-acetone exchange procedure before CO_2 supercritical drying which effectively prevents collapse of the nanostructured aerogels due to capillary forces. Afterward, the dried organic aerogel was carbonized at 800 °C in N_2 for 1 h. Then, the carbonized sample was ground, followed by a second pyrolysis at 950 °C under flowing NH_3 for 30 min. The mass loss during the N_2 and the NH_3 treatment is around 75 wt %. Based on the mass of $FeCl_3$ added and the mass loss during the two pyrolysis steps, the Fe content in the Fe-N-C aerogel catalyst after pyrolysis could be estimated to be around 1.0 wt%. The as-prepared Fe-containing catalysts were denoted as RFMx-800N_2-950NH_3, where x represents the cumulative mass fraction of RFM in the sol. The catalysts are compared to the commercial Pajarito Powder PMF-011904.

2.2 Physicochemical characterization

The morphologies of the catalysts were analysed by scanning electron microscopy (SEM) with a ZEISS SUPRA^{TM} 40 operated at 3.0 kV and transmission electron microscopy (JEOL 2100) operated at 200 kV. Nitrogen sorption isotherms at −196 °C were used to characterize the surface area and pore characteristics of all samples by using a Micromeritics ASAP 2020 instrument. Prior to the measurements, the samples were degassed under 10 mmHg at 200 °C for 8.3 hours. The N_2-adsorption isotherms were used to determine specific surface area (S_{BET}), micropore volume (V_μ), mesopore volume (V_{meso}), total pore volume (V_T) and pore size distribution (PSD). S_{BET} was determined via the Brunauer–Emmett–Teller (BET) equation, and V_T was estimated from the adsorption volume at the relative pressure of 0.995. The Solution of the Adsorption Integral Equation

Using Splines (SAIEUS) program was used for calculating S_{μ}, V_{μ}, V_{meso} and pore size distributions with the 2D-NLDFT-HS model which incorporates energy heterogeneity and geometric corrugation on the surface of carbon pores. X-ray diffraction (XRD) analyses were performed using an X'pert Pro Philips diffractometer equipped with a Cu Kα source (λ = 0.15406 nm) operated at 45 kV and 30 mA. The diffraction angles of the diffraction peaks were determined with High score software. X-ray photoelectron spectroscopy (XPS) was employed to identify the chemical state and determine the atomic concentration of chemical species in all the samples. The measurements were carried out using Thermo Scientific™ K-Alpha™ XPS spectrometer equipped with an Al Kα1,2 monochromatic source (1486.6 eV). All samples were analyzed with a spot size of 200 μm and repetitive tests were conducted on four different spots of all samples to ensure the accuracy of the measurements. A survey spectrum and higher resolution (HR) multiplex scan spectra (C 1s, O 1s, N 1s and Fe 2p core levels) were obtained. Quantification of the elements was carried out with CasaXPS software (Casa Software Ltd.). All HR-spectra were fitted by Gaussian/Lorentzian line shape after a Shirley background removal. Binding energies are referred to the binding energy of the C 1s core level peak at 284.8 eV owing to hydrocarbon contaminants at the surface.

In order to remove impurities and large Fe nanoparticles to increase the durability of catalysts, acid wash (denoted as AW) was performed on the best performing catalyst between the pyrolysis in N_2 atmosphere and the one in NH_3 atmosphere. The acid wash was performed in 0.5 M H_2SO_4 at 80 °C, for 7 h. The XAS measurements at the Fe K-edge from 6912 to 8112 eV were collected at the B18 beamline of the Diamond Light Source, the UK synchrotron facility. Due to the low jump of the transmission edge of the samples, the spectra were collected in the fluorescence mode by means of Ge solid state detector. For each sample, 36 scans were acquired to reach a high signal/noise ratio, each scan lasting ca 4 minutes (total acquisition of about 2 hours per sample). The spectra of the Fe standards, Fe (II) phthalocyanine (Aldrich, Dye content ca. 90%), Fe_3C, Fe_2O_3, iron metal foil, were

acquired in the transmission mode, acquiring 3 repetitions of 3 minutes (total ca. 10 minutes per sample). Standards were prepared as pellets by mixing less than 10 mg of standards with cellulose. The treatment of the data was performed with the ATHENA software [26].

The surface site density (SD) was calculated from CO chemisorption experiments, following a procedure described previously [27]. A known volume of CO is pulsed on the catalyst under study at 193 K every 10 min until detector signal indicates sample CO saturation. Prior to the CO chemisorption experiments, the catalyst was treated at 600 ºC under a N_2 flow for 30 min. Assuming a CO to Fe-N_x surface site stoichiometry of 1:1, the site density can be obtained from the total amount of CO chemisorbed from the following equation 1 [28]:

$$SD_{mass}\,(CO)[sites \cdot g_{cat}^{-1}] = n_{CO}[mol \cdot g^{-1}] \cdot N_A[site \cdot mol^{-1}] \quad \text{(Equation 1)}$$

The turnover frequency (TOF) can be therefore calculated by the following expression [28]:

$$TOF\left[electron \cdot site^{-1} \cdot s^{-1}\right] = \frac{j_M \cdot N_A}{SD_{mass} \cdot F} \quad \text{(Equation 2)}$$

where j_M is the mass activity (in A g^{-1}) at the selected potential, N_A is the Avogadro's number and F is the Faraday constant (96485 C mol^{-1}).

^{57}Fe Mössbauer spectroscopy was used to obtain information on the iron speciation in two down-selected catalysts, with and without acid washing (RFM20-800N_2-950NH_3 and RFM20-800N_2-AW-950NH_3). 120 to 300 mg of catalysts were mounted in a 2 cm^2 holder. The spectra were measured with the sample being at 5 K in a helium flow cryostat (SHI-850 Series from Janis, Woburn, MA, USA) with the Mössbauer spectrometer (Wissel, Germany) operated in the transmission mode with a ^{57}Co/Rh source at room temperature. The velocity driver was operated in the constant acceleration mode with a triangular velocity waveform. The velocity scale and isomer shift (δ_{iso}) were calibrated with the magnetically split sextet of a high-purity α-Fe foil at room temperature. The spectra were fitted with appropriate combinations of Lorentzian profiles with a least-square fitting procedure.

2.3 Electrochemical characterization

All electrochemical tests were conducted using a conventional three-electrode cell at room temperature with a potentiostat/galvanostat from Bio-Logic (HCP-803). A rotating disk electrode (RDE, OrigaTrod), reversible hydrogen electrode (RHE) and graphite electrode were used as working electrode, reference electrode and counter electrode, respectively. For the catalyst ink, 10 mg of catalyst, 46 µL of milliQ-grade H_2O, 752 µL of ethanol and 95 µL of 5 wt% Nafion® solution (Alfa Aesar, 5% w/w in water and 1-propanol) was mixed, then subjected to agitation and sonication alternatively for a total of 1 h. 7 µL of catalysts ink was dropped onto the glassy-carbon electrode (0.196 cm^2), generating a catalyst loading of 0.4 mg cm^{-2}.

All electrochemical tests were conducted in 0.05 M H_2SO_4 aqueous solution. The electrolyte solution was purged with N_2 (or O_2) for 30 min before each test, and N_2 (or O_2) gas flow was kept bubbling in the solution during the measurement in order to maintain the gas atmosphere, but at a slower rate to avoid perturbations. Cyclic voltammetry (CV) between 1.0 and 0 V vs. RHE was conducted in unstirred N_2-saturated solution at a scan rate of 10 mV s^{-1}. CV was performed until stable curves were obtained, in order to remove the impurities and acid-unstable species present in the catalysts. Linear scan voltammograms (LSV) were recorded at five different angular velocities (1600, 1225, 900, 625 and 400 rpm) at 10 mV s^{-1} in the potential range of 0-1.1 V. Koutecky–Levich (K-L) plots were used to calculate the electron-transfer number.

All obtained data was corrected for Ohmic-drop (iR-drop), and all LSVs were corrected by subtracting the background current recorded in N_2-saturated electrolyte. The kinetic current densities of all catalysts were defined by the K-L equation as shown in Equation 3.

$$\frac{1}{j_k} = \frac{1}{j_F} - \frac{1}{j_{lim}} \quad \text{(Equation 3)}$$

where $j_k, j_F \; and \; j_{lim}$ represent the kinetic current density (in mA cm^{-2}), Faradic current density (in mA cm^{-2}) and limiting current density (in mA cm^{-2}), respectively.

The mass activity (in A g^{-1}) was calculated with equation 4 as follows:

$$j_M = -\frac{j_k}{m} \quad \text{(Equation 4)}$$

where j_M (defined > 0) is the mass activity, and m is the catalyst loading (0.4 mg cm^{-2}) on the working electrode.

The number of electrons transferred per O_2 molecule was estimated with the slope of K-L plots (j_F^{-1} vs. $\omega^{-1/2}$), based on equation 5 as follows:

$$\frac{1}{j_F} = \frac{1}{j_k} + \frac{1}{j_{lim}} = \frac{1}{j_k} + \frac{1}{\mathrm{B}\omega^{1/2}} = \frac{1}{j_k} + \frac{1}{\mathrm{B}}\omega^{-1/2}, \text{ and } \mathrm{B} = 0.62\mathrm{nFD}_0^{2/3}\vartheta^{-1/6}C_0^O \quad \text{(Equation 5)}$$

where B^{-1} is the slope of the plot j_F^{-1} vs. $\omega^{-1/2}$, n is the number of electrons transferred, F is the Faraday constant, D_0 (1.93×10^{-5} cm^2 s^{-1}) is the diffusion coefficient of oxygen in 0.05 M H_2SO_4, ϑ is the kinematic viscosity (0.01 cm^2 s^{-1}), C_0^O is the concentration of oxygen in the bulk (1.22×10^{-6} mol cm^{-3}) [29], and ω is the angular rotation frequency (radian s^{-1}, $\omega = 2\pi \times rpm/60$).

Accelerated durability tests (ASTs) were carried out by collecting 2000 cycles at 50 mVs^{-1} between 0.6 and 1.0 V vs. RHE in an N_2 saturated electrolyte to evaluate the stability of the catalysts.

MEAs with an active area of 25 cm^2 were prepared with two different cathode inks. They both contained Nafion® as the ionomer and both suspensions were based on mixtures of water and ethanol. The first ink (ink 1) had a content of Nafion® of around 30 wt% of the dry matter and a large ethanol-to-water ratio of ca. 7 in order to be close to the one used for RDE measurement. The second ink (ink 2) had been modified in order to create a more porous catalytic layer and was based on development work with commercial reference catalysts from Pajarito Powder. This ink had a ratio of 1:1 between the contents of Nafion® and catalyst and an ethanol-to-water ratio of ca. 1. Spray-coated gas-diffusion electrodes (GDEs) with a catalyst loading of 2 mg cm^{-2} were made with each of these two cathode inks. Each of these cathode GDEs was hot-pressed with anode GDE and membrane (the anode GDE was PtRu/C on SGL Sigracet 35 DC GDL (same GDL as for the cathodes), and the membrane was Gore M820.15) to obtain the MEAs. Single-cell testing of the prepared 25-cm^2 MEAs was performed

in a test station and cell holder from Fuel Cell Technologies, Inc., using hydrogen (H_2) and air as the anode and cathode gas stream, respectively. The applied protocol for acquiring I–V characteristic curves was based on US Department of Energy recommendations, and the conditions were a cell temperature of 80 °C, relative humidity of 100 % for both gases, back pressure of either 1.5 or 3.0 bar_{abs} at both the anode and cathode side, and flows of 500 mL min^{-1} and 2000 mL min^{-1} for H_2 and air, respectively.

3 Results and discussion

Figure 1 shows the XRD patterns of Fe-N-C catalysts prepared with different RFM mass ratios with and without the pyrolysis in NH_3 atmosphere. For carbonized catalysts only treated in N_2 atmosphere, only two broad peaks at around 26° and 44° emerge, ascribed to amorphous carbon. After a two-step pyrolysis treatment in N_2 followed by NH_3, two other peaks at 43.6° and 50.8° appear, that can be indexed to (111), (002) planes of γ-Fe (PDF# 96-900-8470). This phase can be formed above 910 °C according to the iron-carbon phase diagram. It is a metastable iron phase at room temperature, but rapid quenching of the material from > 910°C to low temperature can lead to some remaining γ-Fe after synthesis, instead of the more stable α-Fe phase. Besides, it could also be noticed that the intensity of the C (002) peak at 26° increased slightly. This apparent increased graphitic character may be due to the enhanced graphitization at an elevated temperature of 950 °C catalysed by metallic Fe, and to the preferential gasification of disordered carbon during NH_3 pyrolysis [30, 31]. For RFM35 catalysts, the precursors are more concentrated and Fe atoms are more likely to aggregate within the aerogel network then converted to bigger metallic Fe particles after the two-step heat-treatment. Fe nanoparticles act as catalysts that graphitize the adjacent carbon, leading to more intense carbon peaks in RFM35 after the pyrolysis in NH_3. In comparison, RFM 20 and RFM 10 were prepared with RFM and Fe precursors with lower concentrations, enabling a better dispersion

of Fe within aerogel. During the pyrolysis in NH_3, Fe-N_x-C is preferred to be formed instead of crystalline Fe. Less Fe particles lead to less graphitization of carbon scaffold.

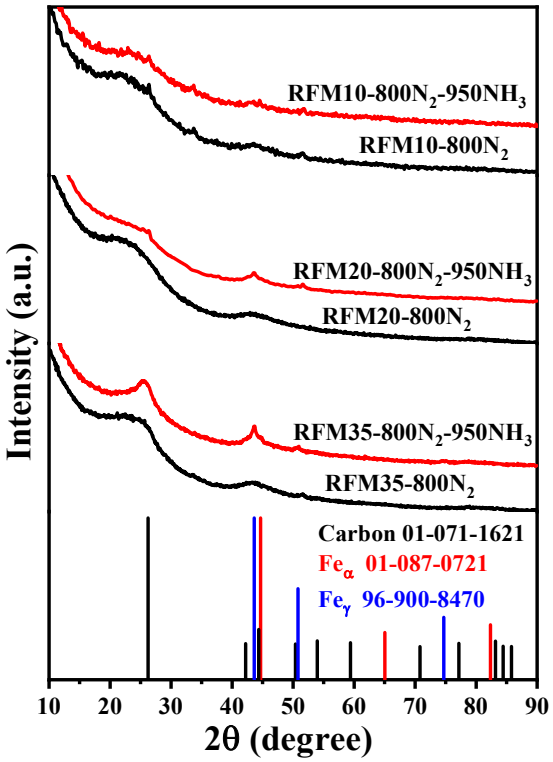

Figure 1 XRD patterns of Fe-N-C catalysts with different RFM mass ratios before and after the pyrolysis in NH_3.

Figure 2 shows the SEM images of Fe-N-C aerogels with various RFM mass ratios before and after pyrolysis in NH_3, namely 35%, 20% and 10%. It can be seen that all samples show a lacy network, resembling the morphology of carbon aerogel from RF resin [32]. The structure of the aerogel catalysts with lower RFM fraction of 10% is looser and more porous, in particular after the pyrolysis in NH_3. Large pores were generated due to the gasification reaction between NH_3 and the carbon framework. On the contrary, the surface of the aerogel prepared with a higher RFM mass ratio of 35% is relatively more compact, and the porosity of the RFM20 is in between. The variation on the morphology of samples with RFM ratio is in line with the work reported by Feng et al [33].

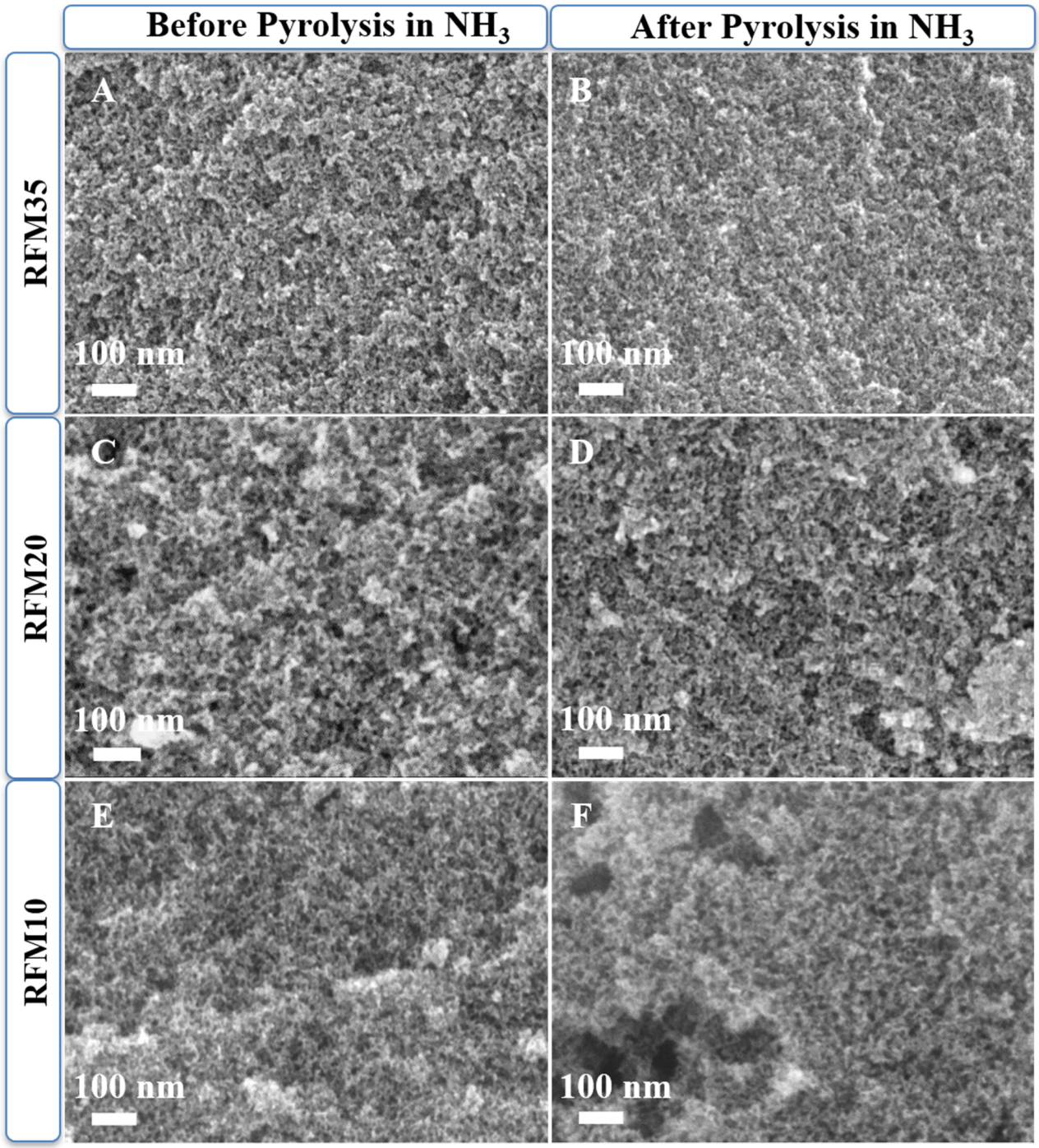

Figure 2 SEM images of Fe-N-C aerogel catalysts prepared with different RFM mass ratios.

The pore characteristics of all samples were investigated by N_2 sorption. Figure 3 exhibits the N_2 adsorption-desorption isotherms and PSD curves of aerogels before and after thermal treatment in NH_3. The textural properties calculated from the nitrogen sorption isotherms are reported in Table 1. Regardless of the pyrolysis conditions under study, all samples show type IV isotherms, including

features associated with micro/mesoporous materials. The isotherm presents a steep rise at low relative pressures and a sharp "knee" in isotherms at around $P/P_o = 0.05$, indicating the presence of micropores. At higher relative pressures, multilayer adsorption begins, followed by capillary condensation accompanied by a hysteresis loop. All Fe-N-C aerogels present H2 hysteresis loops, indicative of interconnected networks containing mesopores of different sizes and shapes.

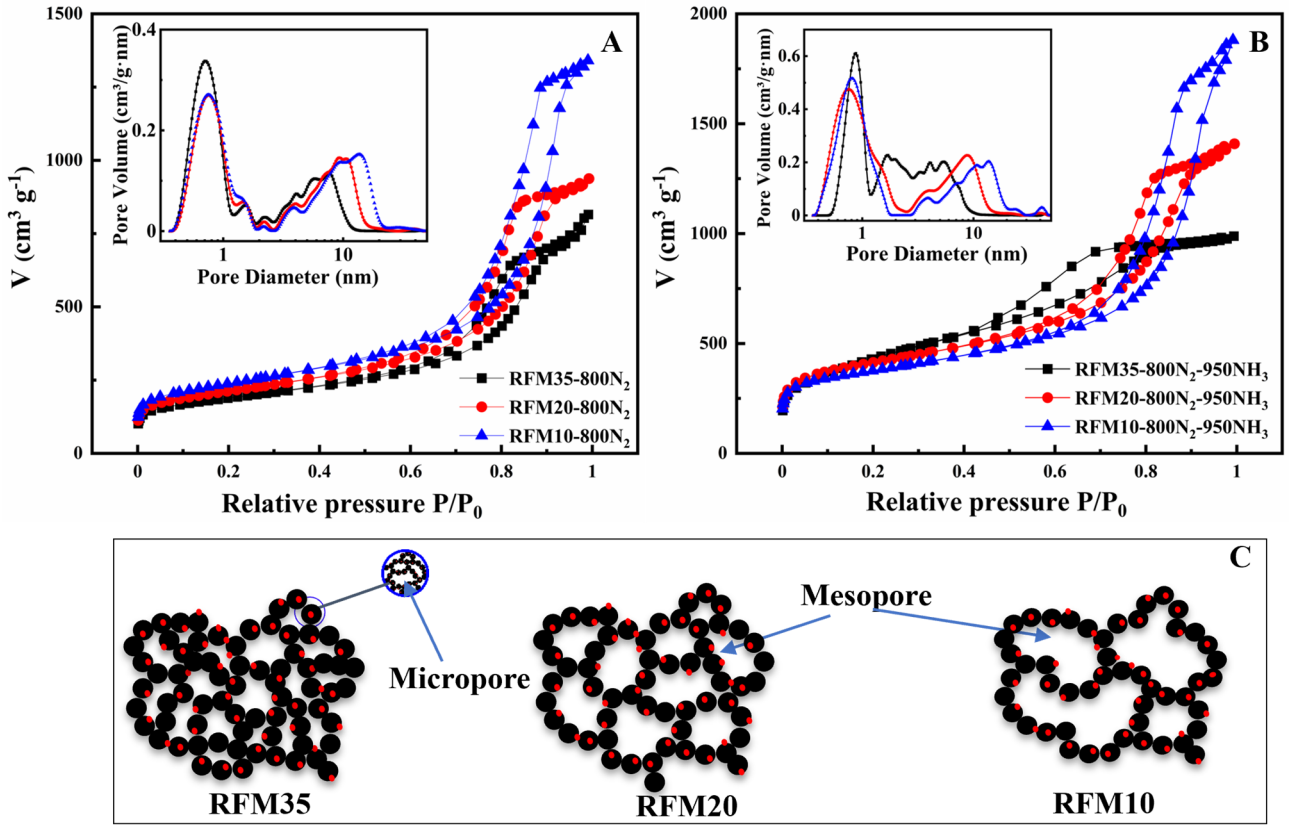

Figure 3 The nitrogen adsorption-desorption isotherms of aerogel catalysts before (A) and after (B) the pyrolysis in NH_3. The insets represent the pore-size distribution of the catalysts. The illustration (C) of Fe-N-C aerogel catalysts with different RFM mass ratios.

As seen from Table 1, it could be noticed that S_{BET} and total pore volumes increase as the RFM mass ratio decreases in the sol. The increase in the total pore volumes is dominantly contributed by the increase in volume of mesopores. Specifically, as the RFM mass ratio decreases from 35% to 10%, the V_{micro} maintains a similar value (~ 0.18 $cm^3\ g^{-1}$), while the V_{meso} increases significantly from 0.67 to 1.85 $cm^3\ g^{-1}$. The same trend applies to the catalysts subjected to the pyrolysis in NH_3, with an

increase of S_{BET} and total porous volume with the NH_3 treatment even though the effect, in this case, is smaller with the decrease of the mass ratio in the sol. These results indicate that the pore characteristic of the resulting Fe-N-C aerogel catalysts is based on the pore structure of the counterpart pyrolyzed exclusively in N_2. The effect of RFM mass ratio on the pore structure is illustrated in Figure 3C. A lower RFM mass ratio implies that a higher fraction of water is entrapped in the pores of the aerogel, which enlarges the average pore size of the final catalysts in the mesopore range. The impact is however milder on the micropores of the resulting pyrolyzed aerogels, which is mainly affected by the pyrolysis conditions and the use or not of a reactive atmosphere [19]. After N_2 atmosphere treatment, from their pore size distribution curves, it can be noticed that the catalysts prepared with a lower RFM mass ratio have a broader pore-size distribution from micropore size up to 20 nm. In contrast, the catalysts with a higher RFM mass ratio of 35% have a narrower pore-size distribution range from 0.36 nm to 10 nm. Upon pyrolysis in NH_3, the pore structure of the aerogels is affected drastically for both micropores and mesopores. The specific surface area (S_{BET}) increases from 710-841 to 1353-1519 $m^2\ g^{-1}$, almost twice as much as their counterpart without NH_3 heat-treatment. The pore volume is also increased from the range of 0.89-2.07 to 1.53 - 2.91 $cm^3\ g^{-1}$. The increase in surface area and pore volume is attributed to the formation of additional micropores and mesopores, which is due to the carbon gasification reaction between NH_3 and carbon matrix composed of the main reaction ($C + NH_3 \rightarrow HCN + H_2$) and a minor reaction ($C + 2H_2 \rightarrow CH_4$) [30].

Table 1 The textural characteristics of the Fe-N-C aerogels prepared by various mass ratios of RFM

Catalyst	S_{BET} ($m^2\ g^{-1}$)	S_{micro} ($m^2\ g^{-1}$)	V_T ($cm^3\ g^{-1}$)	V_{micro} ($cm^3\ g^{-1}$)	V_{meso} ($cm^3\ g^{-1}$)	S_{micro}/S_{BET}	V_{micro}/V_{meso}
RFM35-800N_2	710	465	0.89	0.18	0.67	0.65	0.27
RFM20-800N_2	749	399	1.37	0.17	1.23	0.53	0.14
RFM10-800N_2	841	428	2.07	0.18	1.85	0.51	0.10
RFM35-800N_2-950NH_3	1519	699	1.53	0.36	1.08	0.46	0.33
RFM20-800N_2-950NH_3	1481	877	2.18	0.39	1.71	0.59	0.23
RFM10-800N_2-950NH_3	1353	765	2.91	0.33	2.52	0.57	0.13

To investigate the impact of the RFM mass ratio and pyrolysis conditions on the surface composition of the as-prepared catalysts, XPS analysis was conducted. As shown in Table 2, before heat-treatment in NH_3, only C, N and O are detectable on the surface of the aerogel catalysts, and the variation of the RFM mass ratio did not cause a large change in the surface composition of the resulting catalysts. Comparing the results of catalysts before and after NH_3 heat-treatment, it could be seen that the chemical composition on the surface is largely affected by the pyrolysis conditions, indicated by the change in the Fe and N chemical environment after the heat-treatment in NH_3. This observation agrees with the result in our previous work [19]. Fe particles are encapsulated by layers of graphitized carbon formed during the first heat-treatment in N_2, leading to a lower relative concentration compared with that after pyrolysis in NH_3, as shown from Table 2 and Figure SI.1A and 1B. As for the N 1s spectra (Figure SI.1C and 1D) of all catalysts, they were deconvoluted into five peaks, including pyridinic N (N-6), Fe-N_x, pyrrolic N (N-5), quaternary N (N-Q) and oxidized N (N-O_x) [13]. Their contents for each catalyst under study are listed in Table 2. It could be noticed that the relative contents of pyridinic N and Fe-N_x were slightly increased after the pyrolysis in NH_3, along with the decrease in the relative contents of the other three components. There is growing consensus

that the catalytic sites of Fe-N-C catalyst for the ORR in acid medium can be ascribed to Fe-N_x which leads to the complete reduction of oxygen releasing 4 electrons for catalysts with low Fe content (the content of our catalysts is about 1wt%) [34]. However, several hypotheses on the activity of other N-species for the ORR have also been reported in the literature. Pyridinic N has been widely regarded as another important N-species over the rest N-containing species including N-5, N-Q and N-O_x. It has been demonstrated experimentally and theoretically, that carbon atoms next to pyridinic N with Lewis basicity play a significant role as active sites, to which oxygen molecules are adsorbed as the initial step of the ORR [13].

Table 2 Surface elemental composition of the Fe-N-C catalysts

Catalyst	Fe/C	N/C	O/C	Fe/N	Pyridinic N (N-6)	Fe-Nx	Pyrrolic N (N-5)	Quaternary N (N-Q)	Oxidized N
RFM35-800N_2	0.0006	0.025	0.05	0.02	29.7	20.2	26.5	16.6	7.1
RFM20-800N_2	0.0009	0.024	0.03	0.04	33.8	19.9	29.8	11.2	5.4
RFM10-800N_2	0.0008	0.023	0.05	0.03	28.7	18.0	32.8	13.2	7.4
RFM35-800N_2-950NH_3	0.001	0.034	0.031	0.03	41.5	24.7	19.2	9.1	5.6
RFM20-800N_2-950NH_3	0.0015	0.029	0.030	0.05	38.4	22.8	21.8	10.4	6.5
RFM10-800N_2-950NH_3	0.001	0.027	0.031	0.04	34.9	22.8	25.7	10.9	5.7

From the above physico-chemical characterizations, the pyrolysis in NH_3 has large impact on the microstructure, texture, morphology and chemical composition of the aerogel catalysts, which is in consistent with our previous study [19]. The impact of the pyrolysis in NH_3 on ORR performance of RFM20 catalyst is shown in Figure SI.2. As can be seen from ORR polarization curves and Tafel plots, the catalyst subjected to the pyrolysis in NH_3 exhibits a sharp kinetic-to-diffusion transition region, higher diffusion-limited current density, a flatter plateau in the diffusion-controlled region and higher mass activity (2.9 A g^{-1} vs. 0.14 A g^{-1} at 0.8 V), in comparison with the catalyst without

heat-treatment in NH_3. The impact of the pyrolysis in NH_3 on ORR performance is also consistent with what we have observed in our previous work even though the aerogel catalysts were prepared by different Fe precursors [19]. The enhanced ORR activity of catalysts subjected to the heat-treatment in NH_3 is due to their more interesting features, including higher specific surface area and mesopore volume, higher content of active N-species (mainly N-6 and slightly Fe-N_x).

The electrochemical performance for the ORR of the catalysts with different RFM mass ratios subjected to the pyrolysis in NH_3 was evaluated with RDE in 0.05 M H_2SO_4. Figure 4A exhibits the cyclic voltammograms (CVs) recorded in N_2-saturated electrolyte. All the CVs exhibit a rectangle profile which is typical characteristic of carbonaceous materials, which were the background current used to correct their corresponding ORR polarization currents. Figure 4B exhibits the corrected ORR polarization curves recorded in O_2-saturated electrolyte. As can be seen, the catalysts with lower RFM mass ratio exhibit better mass-transport properties which is verified by a sharp kinetic-to-diffusion transition region, higher diffusion-limited current density and a flatter plateau in the diffusion-controlled regions. The better mass-transport of O_2 in catalysts prepared with low RFM mass ratio is mainly contributed by a higher mesopore volume. Intrinsically, the onset potential for ORR is 0.86 V for the RFM20-800N_2-950NH_3 electrode, whereas for the RFM35-800N_2-950NH_3 and RFM10-800N_2-950NH_3 it is 0.855 V. Furthermore, the half-wave potential of RFM20-800N_2-950NH_3 is 0.763 V, around 10 mV and 90 mV more positive than RFM10-800N_2-950NH_3 and RFM35-800N_2-950NH_3, respectively. Figure 4C compares the Tafel plots. At 0.8V, the RFM20-800N_2-950NH_3 delivers a higher mass activity of 2.9 A g^{-1}, compared to 1.52 and 1.92 A g^{-1} on RFM35-800N_2-950NH_3 and RFM10-800N_2-950NH_3, respectively. The ORR parameters obtained in the present work are close to those reported by Ratso et al [35]. It can be also noticed that the catalysts with RFM mass ratio of 10% and 20% show lower Tafel slopes of 56 mV dec^{-1}, indicating a different mechanism. The electron-transfer number (n) of the catalysts over the potential range of 0.05-0.6 V were further calculated using K-L plots (an example is shown in the inset of Figure 4D) under five different

rotation rates, as shown in Figure 4D. The n values over the potential of 0.05-0.6 V of RFM20-800N_2-950NH_3 and RFM10-800N_2-950NH_3 are in the range of 3.83-3.64 and 4.0-3.75, respectively, indicating the four-electrons pathway dominantly preceded on these two catalysts. As a comparison, the numbers of electrons exchanged for RFM35-800N_2-950NH_3 are lower, 3.17-2.92 over the same potential range. Our best aerogel RFM20-800N_2-950NH_3 is comparable to the commercial Fe-N-C catalyst (Pajarito powder) which delivers a mass activity of 4.11 A g^{-1} with a half-wave potential of 0.753 V and a slightly higher onset potential of 0.88 V.

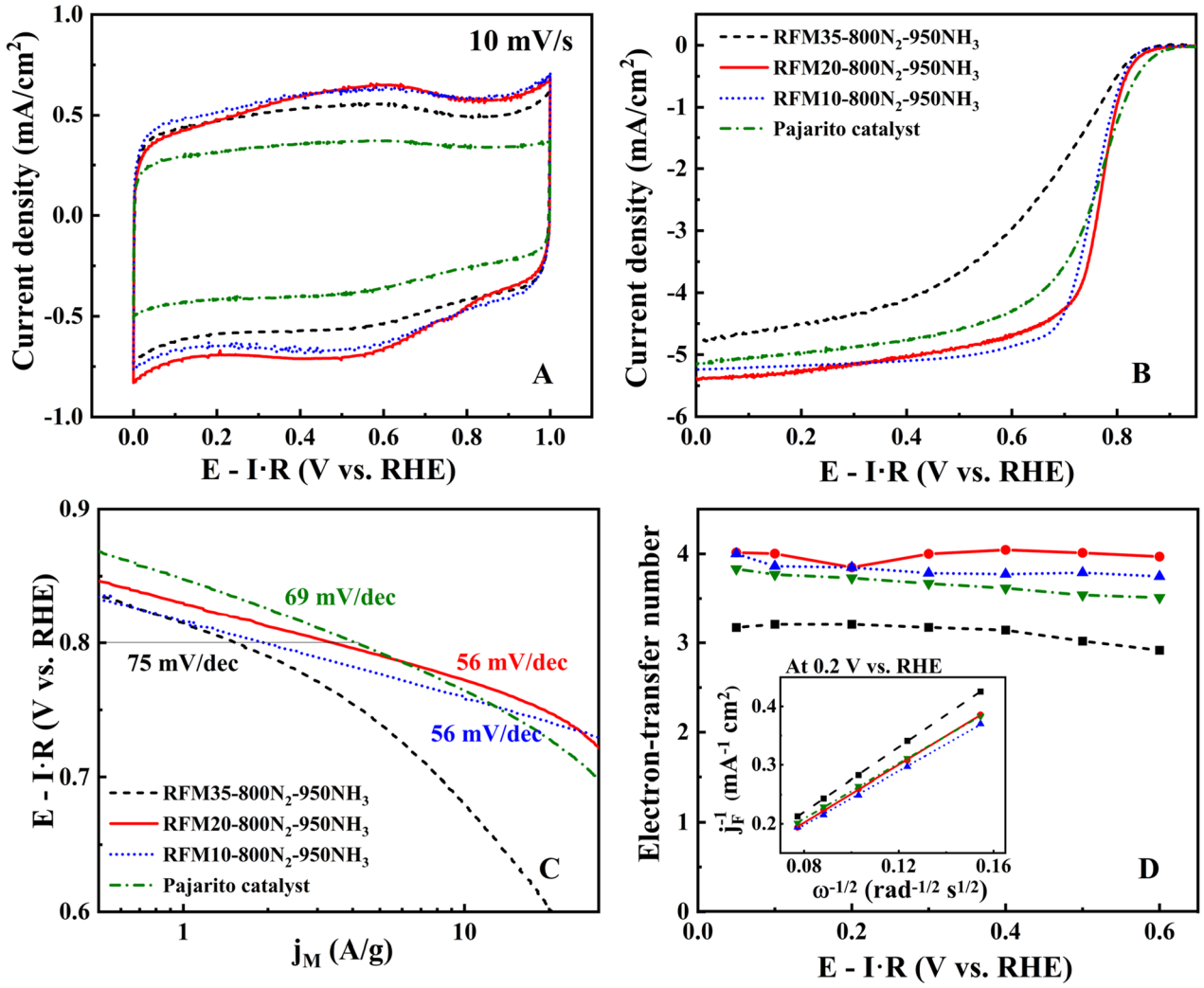

Figure 4 (A) Cyclic voltammograms of catalysts with different RFM mass ratios and commercial Pajarito catalyst recorded in 0.05 M N_2-saturated H_2SO_4 at 10 mV s^{-1}, (B) ORR polarization curves in 0.05 M O_2-saturated H_2SO_4 at 10 mV s^{-1} under 1600 rpm. (C) Tafel plots and (D) Electron-transfer number over 0.05-0.6V. Inset of D: The K-L plots at 0.2 V vs. RHE.

According to the above preliminary results, it could be noted that the catalyst prepared with 20% of RFM mass ratio exhibits the highest catalytic activity for the ORR. For application, the durability is of equal significance as the catalytic activity. Therefore, acid washing treatment (0.5 M H_2SO_4, 80 °C, 7 h) was introduced in the synthesis protocol leading to the initially most active catalyst (namely with the RFM ratio of 20) after the first pyrolysis step in N_2 and before the second one in NH_3, in order to eliminate unstable and inactive or poorly active species such as metallic Fe. The catalyst with acid wash is denoted as RFM20-800N_2-AW-950NH_3, where AW stands for acid washing. In order to identify the Fe species and the effect of acid wash, the catalysts RFM20-800N_2-950NH_3 and RFM20-800N_2-AW-950NH_3 were analysed by Fe edge XAS and ^{57}Fe Mössbauer spectroscopies.

The environment, coordination and oxidation state of the iron atoms and their evolution after acid washing has been studied by measuring the Fe K-edge XAS spectra of RFM20-800N_2-950NH_3 and RFM20-800N_2-AW-950NH_3. Fe-phthalocyanine (with Fe^{2+} coordinated to 4 N atoms in a square planar geometry), Fe_2O_3, Fe_3C and an iron foil were used as standards. The X-ray absorption near edge structure (XANES) for RFM20-800N_2-950NH_3 and RFM20-800N_2-AW-950NH_3 samples, along with the spectra of the standards are shown in Figure 5. The fingerprint comparison with the spectra of the reference samples, suggests that both catalysts contain iron species in $Fe^{2+/3+}$ and Fe^0 oxidation states. As observed, the edge of the spectrum for RFM20-800N_2-AW-950NH_3 shifts towards higher energy with respect to the non-washed sample. This shift is consistent with a higher relative concentration of iron species in 2+/3+ oxidation state relative to zero oxidation state in RFM20-800N_2-AW-950NH_3 than in RFM20-800N_2-950NH_3. This observation agrees with the successful removal of metallic iron species during the acid washing, observed by XRD (see Figure SI.3).

The spectrum for Fe-phthalocyanine (in Figure 5A) shows a pre-edge peak characteristic of Fe atoms in a centro-symmetric square-planar coordination of FeN_4 sites [36]. This peak is not

observed in the spectra of RFM20-800N_2-950NH_3 and RFM20- 800N_2-AW-950NH_3, indicative of either a distorted Fe-N_4 coordination in pyrolyzed catalysts and/or the presence of axial ligands (oxygenated species) on top of Fe-N_4 sites. The latter case is expected for surface-sites. It should be noted though that the absence of the pre-edge peak characteristic for square-planar and centro-symmetric Fe-N_4 is in line with observations in XAS analysis of similar pyrolyzed Fe-N-C catalysts [36, 37] and it can also be assigned to the bending of the FeN_x moieties and/or to the occupation of some of the axial empty positions of the square planar FeN_4 moieties [38]. A careful inspection of the spectrum of RFM20-800N_2-950NH_3 reveals the presence of a feature around 7115 eV, appearing as a shoulder and not a pre-edge peak. This shoulder can also be observed in the spectrum for Fe_3C, and it is therefore indicative of the presence of either iron carbide or metallic Fe (either α or γ as shown below) in RFM20-800N_2-950NH_3.

The phase-corrected k^2-weighted Fourier Transform (FT) of the EXAFS signal is shown in Figure 5B. The FT signal for RFM20-800N_2-950NH_3 presents two peaks at ~ 1.78 Å and 2.27 Å, that can be ascribed to Fe-N/Fe-O and Fe-Fe scatterings, respectively. The Fe-N/Fe-O signal can be assigned to FeN_4 moieties (with O_2 or oxygenated species axially adsorbed on top of Fe) or Fe-O in Fe-oxide. The Fe-Fe signal can be assigned to Fe^0, Fe_3C, or Fe-oxides. However, the Fe-Fe bond length in Fe oxides is expected to lay between ca. 2.8 and 3.4 Å, significantly higher than the values observed here. The lack of intense features at those radial distances in the spectrum for RFM20-800N_2-950NH_3 suggests the absence of well-ordered Fe-oxides, and suggest in turn the assignation of the first shell peak mainly to Fe-N_x species. However, the presence of nanosized and/or amorphous iron oxide particles cannot be excluded, since such particles would display only weak Fe-Fe features in the EXAFS spectrum, as shown by the study of Fe-N-C cathode after operation in PEMFC[39]. The spectrum of RFM20-800N_2-AW-950NH_3 displays a strong signal of the first shell Fe-N (Fe-O) scattering contribution at 1.78 Å. In addition, the spectrum lacks the feature for the Fe-Fe scatterings at ca. 2.27 Å (characteristic for metallic Fe) and which was clearly observed in the spectrum of the

non-washed sample), suggesting the efficient removal during the acid washing of most of the iron metallic and/or iron carbide species.

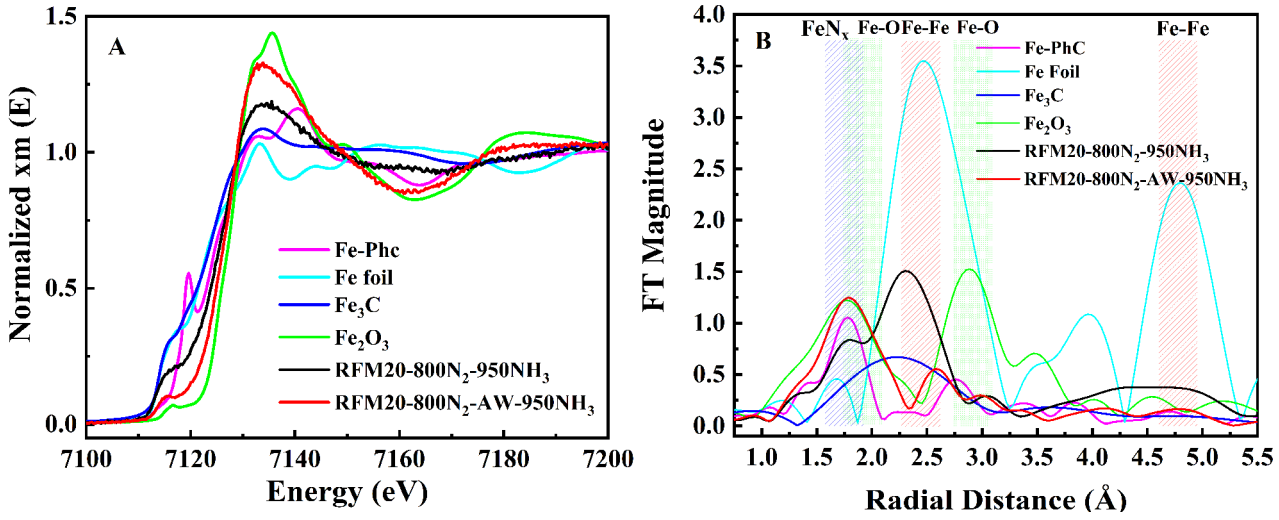

Figure 5. XANES (A) and phase-corrected FT-EXAFS (B) spectra of the catalysts and references under study.

The evolution of the EXAFS signals in the spectra for the non-washed and acid-washed samples is consistent with the qualitative analysis of the XANES spectra and further supports the conclusion that Fe^0 species are removed during the acid washing, whereas Fe-N_x species were stable in RFM20-800N_2-AW-950NH_3. However, the presence of a small feature at 2.6 Å in the spectrum of the acid-washed sample suggests that particles of iron oxide are present in the acid-washed sample.

^{57}Fe Mössbauer spectra were collected at 5K and were fitted with two sextets, one doublet and a singlet, as shown in Figure 6A and Figure 6B. Based on the fitted parameters (Table SI.1), one sextet is unambiguously assigned to iron carbide and the other to ferric oxide while the singlet is assigned to γ-Fe. The doublet is the D1 component widely observed in pyrolyzed Fe–N–C catalysts but only recently assigned to high spin ferric Fe^{3+}-N_x moiety with oxygenated species adsorbed on top [39, 40]. The cumulative relative intensity of zero-valent Fe species (γ-Fe and Fe_3C) decreases from 52 % to 25 % when an intermediate acid washing is performed. One can in particular note the absence of Fe_3C in RFM20-800N_2-AW-950NH_3 while it is present in RFM20-800N_2-950NH_3. In

contrast, the cumulative relative intensity of ferric species (Fe(III)-N_x sites and Fe_2O_3) increases from 47% to 75%. These results confirm the main observations and trends obtained by XRD, XANES and EXAFS. The strong increase in the relative intensity of Fe(III)-N_x sites (D1) from 12 to 28 % can be assigned to the efficient removal of zero-valent Fe species during acid washing. The mild increase of Fe_2O_3 signal intensity from 35 % to 47 % can be the outcome of a) simultaneous removal of zero-valent Fe (increasing the signal of all other Fe species) and of some Fe_2O_3 that was present before the acid washing, or b) simultaneous removal of all Fe_2O_3 that was present before the acid washing and the transformation of some zero-valent Fe (possibly as well as minor fraction of Fe-N_x sites) into Fe_2O_3. The reprecipitation of leached Fe cations on Fe-N-C was recently reported to lead to the operando formation of nanosized Fe_2O_3 spontaneously, both in PEMFC environment and in liquid electrolyte acidic and alkaline environment [39, 41].

These trends could also be confirmed by the TEM images of these catalysts. As seen from Figure 6C and Figure 6D, Fe particles of around 30 nm could be seen in RFM20-800N_2-950NH_3, while they disappear after acid washing. EDX maps of particles confirm the presence of iron particles encapsulated by graphitic carbon or with of a thin oxide layer on the surface (Figure SI.4). TEM did not identify Fe particles in the investigated area of RFM20-800N_2-AW-950NH_3 which may be due to a combination of a small number of large γ-Fe particles (high probability to not find such particle in a small area of catalyst), and the small size and/or amorphous character of Fe_2O_3 particles (possibly 2 nm in size) formed during or after the acid washing.

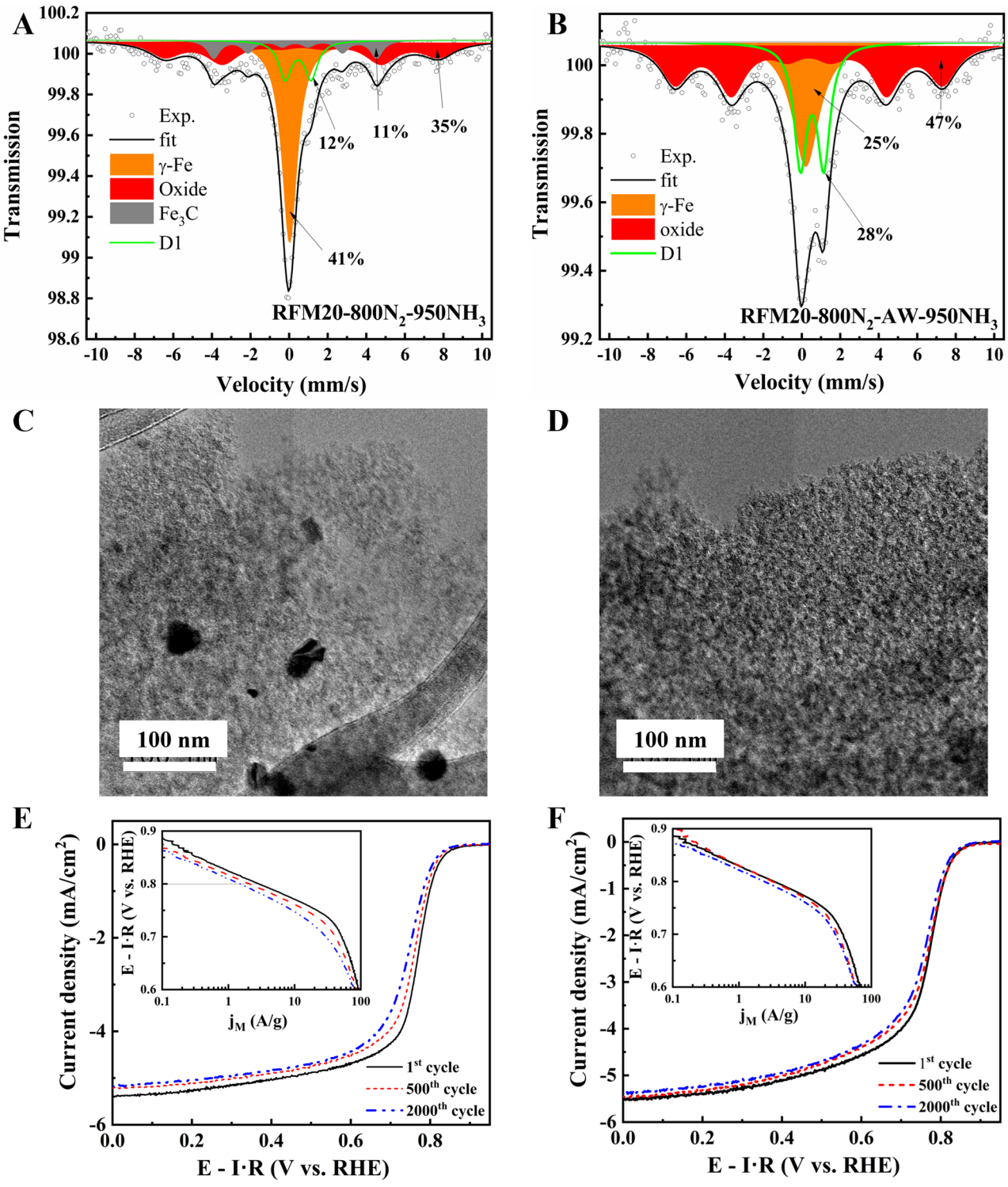

Figure 6 ^{57}Fe Mössbauer spectra, TEM images, LSV curves (Inset: Tafel plots) of RFM20-800N_2-950NH_3 (A, C, E) and RFM20-800N_2-AW-950NH_3 (B, D, F).

Figure 6E and Figure 6F compares the ORR polarization curves and Tafel plots recorded before and after the accelerated durability test for both catalysts (2000 cycles at 50 mVs^{-1} between 0.6 and 1.0 V vs. RHE in an N_2 saturated electrolyte) to evaluate their stability. Before durability test, the catalysts with and without acid washing exhibit the same Tafel slope of 57 mV dec^{-1}, half wave potential of 0.76 V vs. RHE, onset potential of 0.86 V and electron transfer number of ca. 4. The j_M of catalyst with acid washing is 3.29 A g^{-1} which is slightly higher than that without acid washing (2.9 A g^{-1}), still in the line of the results of Ratso et al [42]. This indicates that the acid washing step has minor impact on ORR performance. However, a big influence on the durability could be noticed after acid washing. For the catalyst with acid washing, the ORR polarization curves are almost identical in the kinetic region and the j_M at 0.8V retains 95% of its initial value after AST test of 500 cycles then declines to 70.5% of its initial value after 2000 cycles. By contrast, a negative shift of the polarization curve could be noticed after 500 cycles and the decay of j_M at 0.8V is higher (~ 30%) for the catalysts without acid washing treatment. After 2000 cycles, the decay of j_M for the catalyst without acid washing is higher than 50%. Apparently, acid washing could effectively promote the stability of the Fe-N-C aerogel catalysts.

The number of active sites and turnover frequency (TOF) was calculated on the RFM20-800N_2-AW-950NH_3. The possibility of determining the number of surface-active sites from CO chemisorption has been explored recently by Strasser and co-worker [27]. This approach is based on the observation that the amount of adsorbed CO increased with the ORR activity of Fe-N-C catalysts. Assuming that CO adsorption takes place only at the Fe-N_4 sites located at the catalyst surface with a 1:1 stoichiometry it is possible to determine the site density (SD) from the number of CO molecules chemisorbed from Equation 1 and TOF from equation 2 (see experimental section 2.1). From the CO cryo-chemisorption data we obtained a value of $6.02 \cdot 10^{19}$ surface sites per gram of catalyst for RFM20-800N_2-AW-950NH_3. This value compares well with the highest values reported in literature of $\sim 0.7 \cdot 10^{20}$ surface sites per gram of catalyst [43]. This value translates into a TOF of 0.34 electrons

per site per second calculated for a mass activity of 3.27 A/g at 0.8 V, which in line with the TOF values obtained for Fe-N-C catalysts with similar activities [27, 28, 44].

Single-cell evaluation

Figure 7 shows the single-cell polarisation and power density curves of the RFM20-800N_2-950NH_3 catalyst as cathode with different ink composition and back pressure. The first ink (ink 1) had a content of Nafion® of around 30 wt% of the dry matter and a large ethanol-to-water ratio of ca. 7. The second ink (ink 2) had been modified in several ways to create a more porous catalytic layer, and it had an increased ratio between the contents of Nafion® and catalyst to create a good ionomer network and a decreased ethanol-to-water ratio to ensure good particle dispersion. Regardless of the back pressure, the OCV values are higher for ink 1 than for ink 2. The values obtained at P = 1.5 bar_{abs} are 0.82 V and 0.79 V for ink 1 and ink 2, respectively. The values increase with increasing back pressure, 0.87 V and 0.82 V for ink 1 and ink 2, respectively, at P = 3 bar_{abs}. Nevertheless, the use of ink 2 results in a better performance for both pressures studied, as revealed by the higher voltages for this ink when current is drawn. Indeed, the performance with ink 2 even at low pressure is better than that at higher pressure with ink 1. This is likely an indication that the electrode structure for ink 1 is too compact to enable good transport of gas (oxygen), water and protons, while the electrode structure for ink 2 is better suited for this, as the higher ionomer content here creates more and better paths between the dense particles of catalytic material for the vital mass transport to take place. The gain when increasing the pressure is less significant for ink 2 than for ink 1. This is another indication of the better electrode texture obtained with ink 2, where mass-transport resistances and possible flooding effects – typically revealed at low pressures – are not as severe as for ink 1. However, by comparing the blue and green curves in Figure 7 A and B, one can see that even ink 2 is not free of issues, in as much as the hysteresis in the scans could signify a flooding effect at high current density; however, probably reversible.

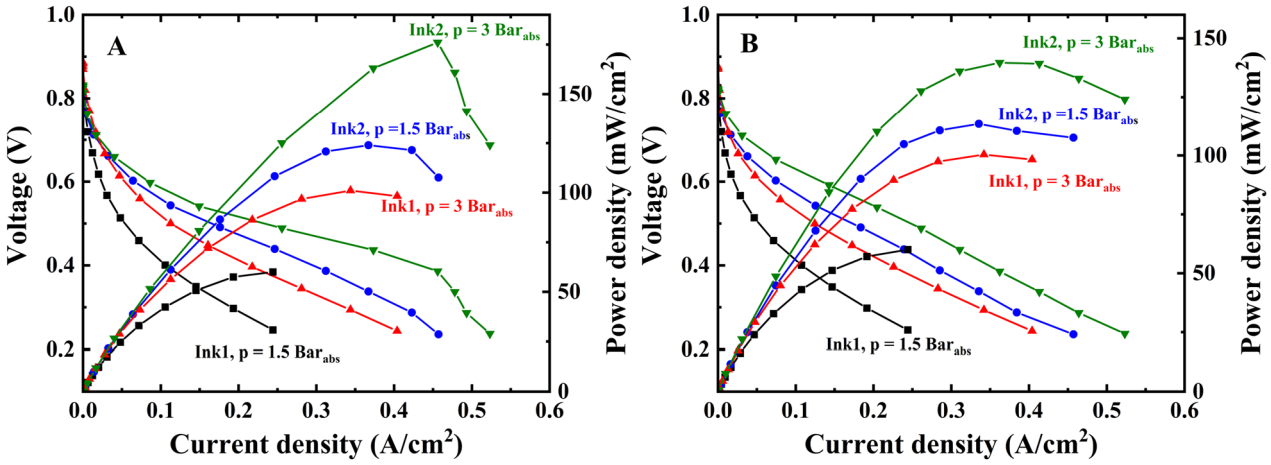

Figure 7. Polarization and power density curves (A: Negative scan, B: Positive scan) for 25-cm² MEAs with cathodes made from two different inks. Ink 1: Ionomer/catalyst (I/C) ratio 0.47, EtOH/H_2O ratio 7.2; Ink 2: I/C ratio 1.0, EtOH/H_2O ratio ca. 1. Cathode catalyst loading: 2 mg cm^{-2}. Test conditions: 80 °C; H_2/air at 500/2000 mL min^{-1}, 100 % RH, and back pressure of 1.5 or 3 bar$_{abs}$

These results emphasise that the intrinsic characteristics of the material with good performance in RDE could not guarantee a good performance in PEMFC. MEA implementation conditions, the texture of the catalytic layer, the ink recipe as well as the hydrophobicity degree of the whole electrode determine the utilization of the active sites of catalyst and the flooding conditions of the electrodes. All these parameters need to be adapted to the catalyst characteristics particularly for PGM-free Fe-N-C-based catalysts. Due to their lower activity compared to Pt/C based catalysts, the quantity of the PGM-free Fe/N/C-based catalysts has to be increased leading to a thicker catalyst layer and the texture of this layer has to be adapted. Here we have already found that at 0.5 V, for P = 3 bar$_{abs}$, the current density can be doubled (from 0.116 A cm^{-2} to 0.258 A cm^{-2}), while it can even be multiplied by four at P = 1.5 bar$_{abs}$ (from 0.047 A cm^{-2} to 0.180 A cm^{-2}), by adapting the ink composition (see Figure 7). This maximum power value of our catalyst is higher than the value obtained for non-ZIF derived Fe-based catalysts [37, 45] and the catalysts cited by Shao et al [2] measured in H_2/air fuel cells. However, compared with the commercial Pajarito powder tested in our study (ink 2, see Figure SI.5) and some state-of-the-art Fe-N-C cathodes reported in the literature, as can been from the Table SI.2, there is still a certain gap and a further improvement is needed for our Fe-N-C aerogel catalyst [18,

46, 47]. It is clear that our Fe-N-C aerogel catalyst has not been extensively studied like the others (Pajarito and ZIF-based Fe-N-C catalysts), and thus further optimisation on the ink and manufacturing conditions for MEAs with this particular catalyst is likely to yield still better performances.

4 Conclusion

Fe-N-C aerogel catalysts were prepared by sol–gel reaction of resorcinol, melamine, formaldehyde and $FeCl_3$ salt, supercritical drying and thermal treatments. The characteristics of the resultant catalysts can be tailored and adjusted to the catalyst specificities by modifying the chemical or process parameters. The texture of catalysts can be modified by varying the mass ratio of monomer in the sol. The lower the ratio in the initial sol-gel step, the higher quantity of pores with large size. By applying a NH_3 thermal treatment, the increasing in surface area and pore volume is attributed to the formation of both micropores and mesopores due to the carbon gasification reaction between NH_3 and the carbon matrix. Likewise, the variation of the RFM mass ratio did not modify the surface composition which is mainly affected by the heat-treatment gas atmosphere. The NH_3 thermal treatment largely affects the surface composition, specifically on the N chemical environment on the surface of the catalysts. The contents of pyridinic N and Fe-N_x were increased for the catalysts with heat treatment in NH_3. The catalyst with a mass ratio of 20% treated in NH_3 exhibits the best ORR performance (activity and mass transport) due to the optimum balance between pore structure and active N species. Through acid washing, the durability of this catalyst was further improved by eliminating the unstable and inactive species (metallic iron and iron carbides, and confirmed by conclusions coming from XRD, TEM, XANES, FT-EXAFS and Mössbauer) preserving Fe-N_x moieties responsible for the high activity measured for the oxygen reduction reaction in acid electrolyte. From the CO cryo-chemisorption on RFM20-800N_2-AW-950NH_3, the number of surface sites are comparable to the highest values reported in literature and a turnover frequency (TOF) is in line with the TOF values obtained for Fe-N-C catalysts with similar activities. The catalyst was

implemented in 25-cm² surface area MEAs with different ink recipes and compared in single cell. It was found that the performance is not only affected by the intrinsic characteristics of the catalyst but also the ink formula for the catalyst layer. The formula of the ink has to be adapted to the characteristics of the catalyst in order to achieve a good performance.

Acknowledgements

The authors wish to thank Pierre Ilbizian (PERSEE-MINES ParisTech) for help with supercritical drying, Suzanne Jacomet for SEM analysis, Gabriel Monge for XRD measurements, Frédéric Georgi for XPS measurements (CEMEF-MINES ParisTech), and Laetitia Dubau for TEM and EDX analysis (CNRS/LEPMI).

Funding: This project has received funding from the Fuel Cells and Hydrogen 2 Joint Undertaking under the European Union's Horizon 2020 research and innovation program under grant agreement No. 779550 (project PEGASUS).

References

[1] Y. Nie, L. Li, Z. Wei, Recent advancements in Pt and Pt-free catalysts for oxygen reduction reaction, Chemical Society Reviews, 44 (2015) 2168-2201. https://doi.org/10.1039/c4cs00484a.
[2] M. Shao, Q. Chang, J.P. Dodelet, R. Chenitz, Recent Advances in Electrocatalysts for Oxygen Reduction Reaction, Chemical Reviews, 116 (2016) 3594-3657. https://doi.org/10.1021/acs.chemrev.5b00462.
[3] F. Jaouen, E. Proietti, M. Lefèvre, R. Chenitz, J.-P. Dodelet, G. Wu, H.T. Chung, C.M. Johnston, P. Zelenay, Recent advances in non-precious metal catalysis for oxygen-reduction reaction in polymer electrolyte fuelcells, Energy & Environmental Science, 4 (2011) 114-130. https://doi.org/10.1039/c0ee00011f.
[4] D. Liu, L. Tao, D. Yan, Y. Zou, S. Wang, Recent Advances on Non-precious Metal Porous Carbon-based Electrocatalysts for Oxygen Reduction Reaction, ChemElectroChem, 5 (2018) 1775-1785. https://doi.org/10.1002/celc.201800086.
[5] Y. Nabae, A. Ishihara, Recent Progress in Non-precious Metal Fuel Cell Catalysts, in: Nanocarbons for Energy Conversion: Supramolecular Approaches, 2019, pp. 253-276.
[6] A.A. Gewirth, J.A. Varnell, A.M. DiAscro, Nonprecious Metal Catalysts for Oxygen Reduction in Heterogeneous Aqueous Systems, Chemical Reviews, 118 (2018) 2313-2339. https://doi.org/10.1021/acs.chemrev.7b00335.
[7] L. Zhang, D.P. Wilkinson, Y. Liu, J. Zhang, Progress in nanostructured (Fe or Co)/N/C non-noble metal electrocatalysts for fuel cell oxygen reduction reaction, Electrochimica Acta, 262 (2018) 326-336. https://doi.org/10.1016/j.electacta.2018.01.046.

[8] K. Mamtani, D. Singh, J. Tian, J.-M.M. Millet, J.T. Miller, A.C. Co, U.S. Ozkan, Evolution of N-Coordinated Iron–Carbon (FeNC) Catalysts and Their Oxygen Reduction (ORR) Performance in Acidic Media at Various Stages of Catalyst Synthesis: An Attempt at Benchmarking, Catalysis Letters, 146 (2016) 1749-1770. https://doi.org/10.1007/s10562-016-1800-z.
[9] F. Jaouen, D. Jones, N. Coutard, V. Artero, P. Strasser, A. Kucernak, Toward Platinum Group Metal-Free Catalysts for Hydrogen/Air Proton-Exchange Membrane Fuel Cells, Johnson Matthey Technology Review, 62 (2018) 231-255. https://doi.org/10.1595/205651318x696828.
[10] A. Zitolo, V. Goellner, V. Armel, M.T. Sougrati, T. Mineva, L. Stievano, E. Fonda, F. Jaouen, Identification of catalytic sites for oxygen reduction in iron- and nitrogen-doped graphene materials, Nature Materials, 14 (2015) 937-942. https://doi.org/10.1038/nmat4367.
[11] Q. Jia, N. Ramaswamy, U. Tylus, K. Strickland, J. Li, A. Serov, K. Artyushkova, P. Atanassov, J. Anibal, C. Gumeci, Spectroscopic insights into the nature of active sites in iron–nitrogen–carbon electrocatalysts for oxygen reduction in acid, Nano Energy, 29 (2016) 65-82. https://doi.org/10.1016/j.nanoen.2016.03.025.
[12] E. Proietti, F. Jaouen, M. Lefevre, N. Larouche, J. Tian, J. Herranz, J.P. Dodelet, Iron-based cathode catalyst with enhanced power density in polymer electrolyte membrane fuel cells, Nature communications, 2 (2011) 416. https://doi.org/10.1038/ncomms1427.
[13] J. Li, S. Ghoshal, W. Liang, M.-T. Sougrati, F. Jaouen, B. Halevi, S. McKinney, G. McCool, C. Ma, X. Yuan, Structural and mechanistic basis for the high activity of Fe–N–C catalysts toward oxygen reduction, Energy & Environmental Science, 9 (2016) 2418-2432. https://doi.org/10.1039/c6ee01160h.
[14] A. Serov, M.H. Robson, K. Artyushkova, P. Atanassov, Templated non-PGM cathode catalysts derived from iron and poly(ethyleneimine) precursors, Applied Catalysis B: Environmental, 127 (2012) 300-306. https://doi.org/10.1016/j.apcatb.2012.08.040.
[15] R. Gokhale, Y. Chen, A. Serov, K. Artyushkova, P. Atanassov, Novel dual templating approach for preparation of highly active Fe-N-C electrocatalyst for oxygen reduction, Electrochimica Acta, 224 (2017) 49-55. https://doi.org/10.1016/j.electacta.2016.12.052.
[16] A. Serov, K. Artyushkova, P. Atanassov, Fe-N-C Oxygen Reduction Fuel Cell Catalyst Derived from Carbendazim: Synthesis, Structure, and Reactivity, Advanced Energy Materials, 4 (2014) 1301735. https://doi.org/10.1002/aenm.201301735.
[17] A. Serov, M.H. Robson, B. Halevi, K. Artyushkova, P. Atanassov, Highly active and durable templated non-PGM cathode catalysts derived from iron and aminoantipyrine, Electrochemistry Communications, 22 (2012) 53-56. https://doi.org/10.1016/j.elecom.2012.04.029.
[18] X. Yang, Y. Wang, G. Zhang, L. Du, L. Yang, M. Markiewicz, J.-y. Choi, R. Chenitz, S. Sun, SiO_2-Fe/N/C catalyst with enhanced mass transport in PEM fuel cells, Applied Catalysis B: Environmental, 264 (2020) 118523. https://doi.org/10.1016/j.apcatb.2019.118523.
[19] Y. Wang, S. Berthon-Fabry, One-Pot Synthesis of Fe-N-Containing Carbon Aerogel for Oxygen Reduction Reaction, Electrocatalysis, 12 (2021) 78-90. https://doi.org/10.1007/s12678-020-00633-8.
[20] W. Kiciński, J.P. Sęk, A. Kowalczyk, S.T. Surdacka, A.M. Nowicka, S. Dyjak, B. Budner, M. Donten, Fe–N–C catalysts for oxygen electroreduction under external magnetic fields: Reduction of magnetic O_2 to nonmagnetic H_2O, Journal of Energy Chemistry, (2021) 296-308. https://doi.org/10.1016/j.jechem.2021.04.048.
[21] A. Sarapuu, K. Kreek, K. Kisand, M. Kook, M. Uibu, M. Koel, K. Tammeveski, Electrocatalysis of oxygen reduction by iron-containing nitrogen-doped carbon aerogels in alkaline solution, Electrochimica Acta, 230 (2017) 81-88. https://doi.org/10.1016/j.electacta.2017.01.157.
[22] S. Liu, C. Deng, L. Yao, H. Zhong, H. Zhang, The key role of metal dopants in nitrogen-doped carbon xerogel for oxygen reduction reaction, Journal of Power Sources, 269 (2014) 225-235. https://doi.org/10.1016/j.jpowsour.2014.06.148.

[23] K. Elumeeva, J. Ren, M. Antonietti, T.-P. Fellinger, High Surface Iron/Cobalt-Containing Nitrogen-Doped Carbon Aerogels as Non-Precious Advanced Electrocatalysts for Oxygen Reduction, ChemElectroChem, 2 (2015) 584-591. https://doi.org/10.1002/celc.201402364.
[24] N. Zion, D.A. Cullen, P. Zelenay, L. Elbaz, Heat‐Treated Aerogel as a Catalyst for the Oxygen Reduction Reaction, Angew. Chem. Int. Ed., 59 (2020) 2483-2489. https://doi.org/10.1002/anie.201913521.
[25] G. Rasines, P. Lavela, C. Macías, M.C. Zafra, J.L. Tirado, J.B. Parra, C.O. Ania, N-doped monolithic carbon aerogel electrodes with optimized features for the electrosorption of ions, Carbon, 83 (2015) 262-274. https://doi.org/10.1016/j.carbon.2014.11.015.
[26] B. Ravel, M. Newville, ATHENA, ARTEMIS, HEPHAESTUS: data analysis for X-ray absorption spectroscopy using IFEFFIT, Journal of synchrotron radiation, 12 (2005) 537-541. https://doi.org/10.1107/S0909049505012719.
[27] N.R. Sahraie, U.I. Kramm, J. Steinberg, Y. Zhang, A. Thomas, T. Reier, J.-P. Paraknowitsch, P. Strasser, Quantifying the density and utilization of active sites in non-precious metal oxygen electroreduction catalysts, Nature communications, 6 (2015) 1-9. https://doi.org/10.1038/ncomms9618.
[28] M. Primbs, Y. Sun, A. Roy, D. Malko, A. Mehmood, M.-T. Sougrati, P.-Y. Blanchard, G. Granozzi, T. Kosmala, G. Daniel, P. Atanassov, J. Sharman, C. Durante, A. Kucernak, D. Jones, F. Jaouen, P. Strasser, Establishing reactivity descriptors for platinum group metal (PGM)-free Fe–N–C catalysts for PEM fuel cells, Energy & Environmental Science, 13 (2020) 2480-2500. https://doi.org/10.1039/d0ee01013h.
[29] W. Xing, M. Yin, Q. Lv, Y. Hu, C. Liu, J. Zhang, Oxygen Solubility, Diffusion Coefficient, and Solution Viscosity, in: Rotating Electrode Methods and Oxygen Reduction Electrocatalysts, 2014, pp. 1-31.
[30] F. Jaouen, F. Charreteur, J.P. Dodelet, Fe-Based Catalysts for Oxygen Reduction in PEMFCs, Journal of The Electrochemical Society, 153 (2006) A689-A698. https://doi.org/10.1149/1.2168418.
[31] K. Strickland, E. Miner, Q. Jia, U. Tylus, N. Ramaswamy, W. Liang, M.T. Sougrati, F. Jaouen, S. Mukerjee, Highly active oxygen reduction non-platinum group metal electrocatalyst without direct metal-nitrogen coordination, Nat Commun, 6 (2015) 7343. https://doi.org/10.1038/ncomms8343.
[32] C.I. Merzbacher, S.R. Meier, J.R. Pierce, M.L. Korwin, Carbon aerogels as broadband non-reflective materials, Journal of non-crystalline solids, 285 (2001) 210-215. https://doi.org/10.1016/S0022-3093(01)00455-0.
[33] S.A. Al‐Muhtaseb, J.A. Ritter, Preparation and properties of resorcinol‐formaldehyde organic and carbon gels, Advanced materials, 15 (2003) 101-114. https://doi.org/10.1002/adma.200390020.
[34] K. Kumar, P. Gairola, M. Lions, N. Ranjbar-Sahraie, M. Mermoux, L. Dubau, A. Zitolo, F. Jaouen, F. Maillard, Physical and chemical considerations for improving catalytic activity and stability of non-precious-metal oxygen reduction reaction catalysts, ACS Catalysis, 8 (2018) 11264-11276. https://doi.org/10.1021/acscatal.8b02934.
[35] S. Ratso, N. Ranjbar Sahraie, M.T. Sougrati, M. Käärik, M. Kook, R. Saar, P. Paiste, Q. Jia, J. Leis, S. Mukerjee, F. Jaouen, K. Tammeveski, Synthesis of highly-active Fe–N–C catalysts for PEMFC with carbide-derived carbons, Journal of Materials Chemistry A, 6 (2018) 14663-14674. https://doi.org/10.1039/c8ta02325e.
[36] M.M. Alves, J. Dodelet, D. Guay, M. Ladouceur, G. Tourillon, Origin of the electrocatalytic properties for oxygen reduction of some heat-treated polyacrylonitrile and phthalocyanine cobalt compounds adsorbed on carbon black as probed by electrochemistry and X-ray absorption spectroscopy, The Journal of Physical Chemistry, 96 (1992) 10898-10905. https://doi.org/10.1021/j100205a054.

[37] Á. García, M. Retuerto, C. Dominguez, L. Pascual, P. Ferrer, D. Gianolio, A. Serrano, P. Assmann, D.G. Sanchez, M.A. Pena, Fe doped porous triazine as efficient electrocatalysts for the oxygen reduction reaction in acid electrolyte, Applied Catalysis B: Environmental, 264 (2020) 118507. https://doi.org/10.1016/j.apcatb.2019.118507.
[38] H. Fei, J. Dong, Y. Feng, C.S. Allen, C. Wan, B. Volosskiy, M. Li, Z. Zhao, Y. Wang, H. Sun, General synthesis and definitive structural identification of MN_4C_4 single-atom catalysts with tunable electrocatalytic activities, Nature Catalysis, 1 (2018) 63-72. https://doi.org/10.1038/s41929-017-0008-y.
[39] J. Li, M.T. Sougrati, A. Zitolo, J.M. Ablett, I.C. Oğuz, T. Mineva, I. Matanovic, P. Atanassov, Y. Huang, I. Zenyuk, Identification of durable and non-durable FeN x sites in Fe–N–C materials for proton exchange membrane fuel cells, Nature Catalysis, 4 (2021) 10-19. https://doi.org/10.1038/s41929-020-00545-2.
[40] T. Mineva, I. Matanovic, P. Atanassov, M.-T. Sougrati, L. Stievano, M. Clémancey, A. Kochem, J.-M. Latour, F. Jaouen, Understanding Active Sites in Pyrolyzed Fe–N–C Catalysts for Fuel Cell Cathodes by Bridging Density Functional Theory Calculations and 57Fe Mössbauer Spectroscopy, ACS Catalysis, 9 (2019) 9359-9371. https://doi.org/10.1021/acscatal.9b02586.
[41] Á. García, L. Pascual, P. Ferrer, D. Gianolio, G. Held, D.C. Grinter, M.A. Peña, M. Retuerto, S. Rojas, Study of the evolution of FeN_xC_y and Fe_3C species in Fe/N/C catalysts during the oxygen reduction reaction in acid and alkaline electrolyte, Journal of Power Sources, 490 (2021) 229487. https://doi.org/10.1016/j.jpowsour.2021.229487.
[42] S. Ratso, M.T. Sougrati, M. Käärik, M. Merisalu, M. Rähn, V. Kisand, A. Kikas, P. Paiste, J. Leis, V. Sammelselg, F. Jaouen, K. Tammeveski, Effect of Ball-Milling on the Oxygen Reduction Reaction Activity of Iron and Nitrogen Co-doped Carbide-Derived Carbon Catalysts in Acid Media, ACS Applied Energy Materials, 2 (2019) 7952-7962. https://doi.org/10.1021/acsaem.9b01430.
[43] S. Specchia, P. Atanassov, J.H. Zagal, Mapping transition metal–nitrogen–carbon catalyst performance on the critical descriptor diagram, Current Opinion in Electrochemistry, 27 (2021) 100687. https://doi.org/10.1016/j.coelec.2021.100687.
[44] N.D. Leonard, S. Wagner, F. Luo, J. Steinberg, W. Ju, N. Weidler, H. Wang, U.I. Kramm, P. Strasser, Deconvolution of utilization, site density, and turnover frequency of Fe–nitrogen–carbon oxygen reduction reaction catalysts prepared with secondary N-precursors, ACS Catalysis, 8 (2018) 1640-1647. https://doi.org/10.1021/acscatal.7b02897.
[45] Y. Hu, J.O. Jensen, W. Zhang, S. Martin, R. Chenitz, C. Pan, W. Xing, N.J. Bjerrum, Q. Li, Fe_3C-based oxygen reduction catalysts: synthesis, hollow spherical structures and applications in fuel cells, Journal of Materials Chemistry A, 3 (2015) 1752-1760. https://doi.org/10.1039/c4ta03986f.
[46] Y. Chen, S. Ji, S. Zhao, W. Chen, J. Dong, W.C. Cheong, R. Shen, X. Wen, L. Zheng, A.I. Rykov, S. Cai, H. Tang, Z. Zhuang, C. Chen, Q. Peng, D. Wang, Y. Li, Enhanced oxygen reduction with single-atomic-site iron catalysts for a zinc-air battery and hydrogen-air fuel cell, Nat Commun, 9 (2018) 5422. https://doi.org/10.1038/s41467-018-07850-2.
[47] H.T. Chung, D.A. Cullen, D. Higgins, B.T. Sneed, E.F. Holby, K.L. More, P. Zelenay, Direct atomic-level insight into the active sites of a high-performance PGM-free ORR catalyst, Science, 357 (2017) 479-484. https://doi.org/10.1126/science.aan2255.

Supporting information

Influence of the synthesis parameters on the Proton Exchange Membrane Fuel Cells performance of Fe-N-C aerogel catalysts

Youling Wang [a], Mikkel J. Larsen [b], Sergio Rojas [c], Moulay-Tahar Sougrati,[d] Frédéric Jaouen [d], Pilar Ferrer[e], Diego Gianolio[e], Sandrine Berthon-Fabry [a,*]

[a] MINES ParisTech, PSL University, Centre procédés, énergies renouvelables et systèmes énergétiques (PERSEE) CS 10207 rue Claude Daunesse, 06904, Sophia Antipolis Cedex, France

[b] IRD Fuel Cells A/S, Emil Neckelmanns Vej 15 A&B, DK-5220 Odense SØ, Denmark

[c] Grupo de Energía y Química Sostenibles, Instituto de Catálisis y Petroleoquímca, CSIC, Marie Curie 2, 28049, Madrid, Spain

[d] ICGM, Univ. Montpellier, CNRS, ENSCM, Montpellier, France

[e]Diamond Light Source, Harwell Science and Innovation Campus, Didcot, OX11 0DE, UK

*Corresponding author.

E-mail address: sandrine.berthon-fabry@mines-paristech.fr (S. Berthon-Fabry). Tel: +33 493957547

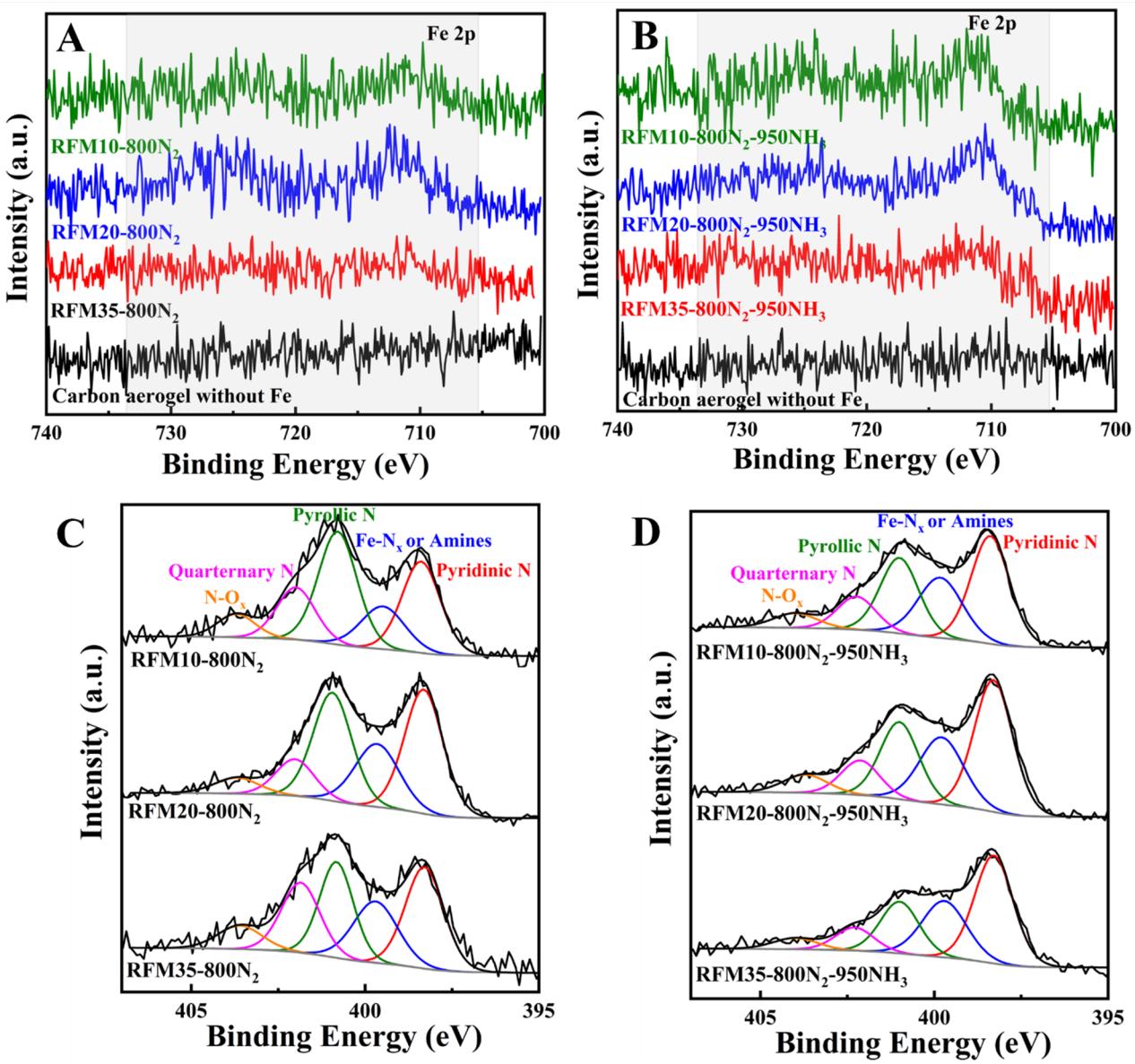

Figure SI.1 High-resolution XPS spectra of Fe2p (A, B) and N 1s (C, D) of Fe-N-C aerogels before and after NH_3 heat treatment.

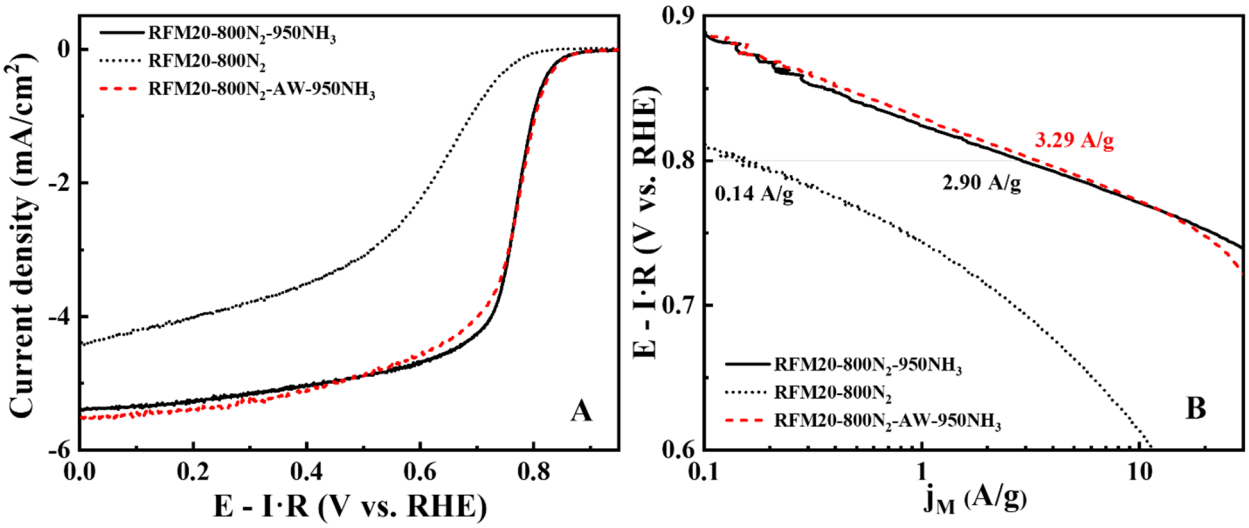

Figure SI.2 LSV curves in 0.05 M O_2-saturated H_2SO_4 at 10 mV s^{-1} under 1600 rpm (A) and Tafel plots (B) of RFM20 catalysts with and without pyrolysis in NH_3, and with acid washing and pyrolysis in NH_3.

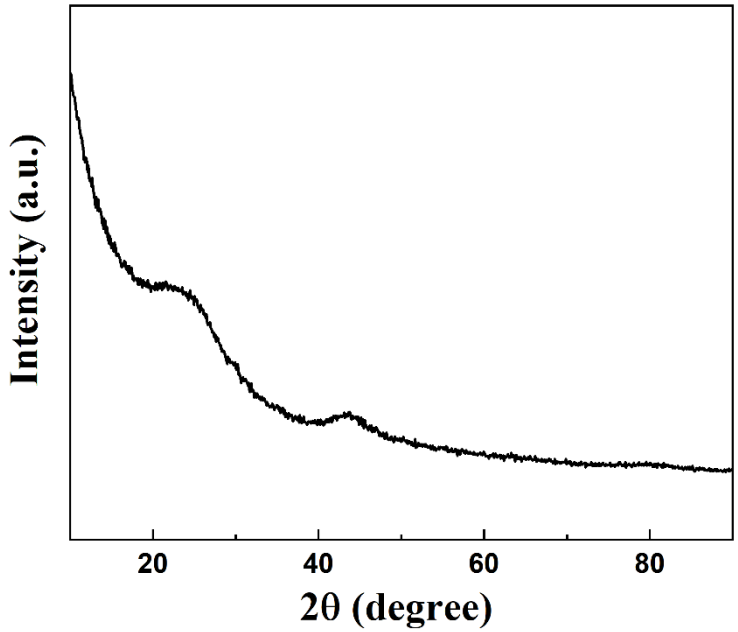

Figure SI.3 XRD pattern of RFM20-800N_2-AW-950NH_3.

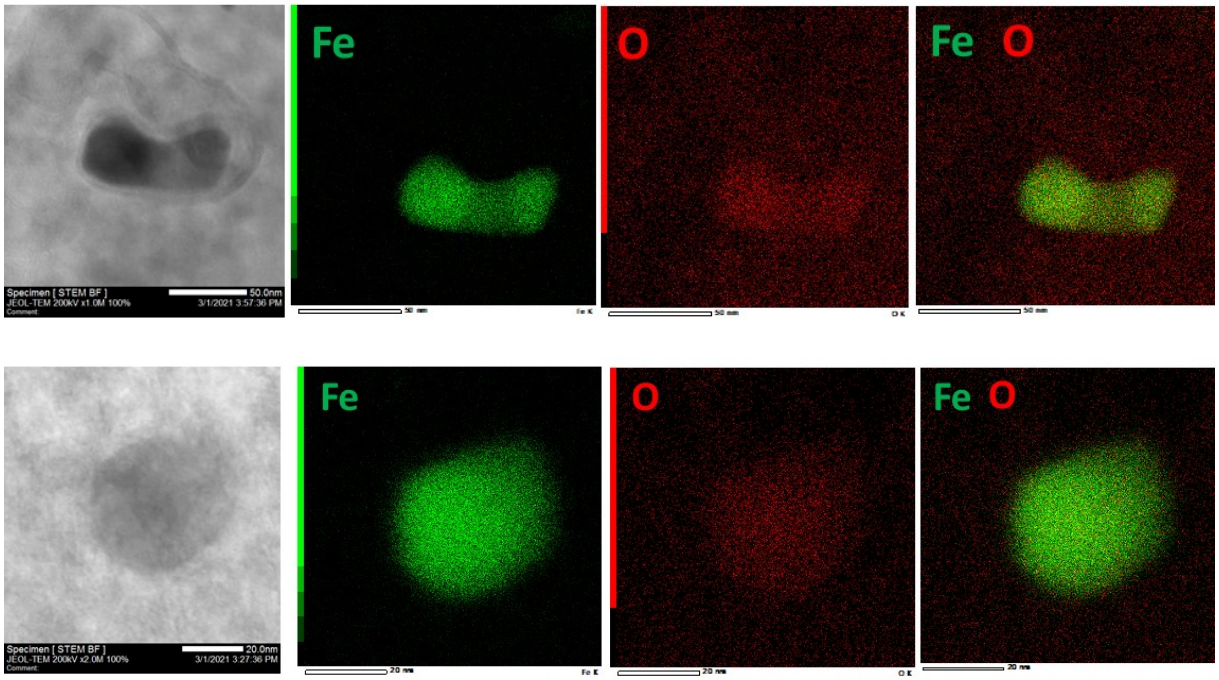

Figure SI.4 EDX maps of particles on RFM20-800N_2-950NH_3.

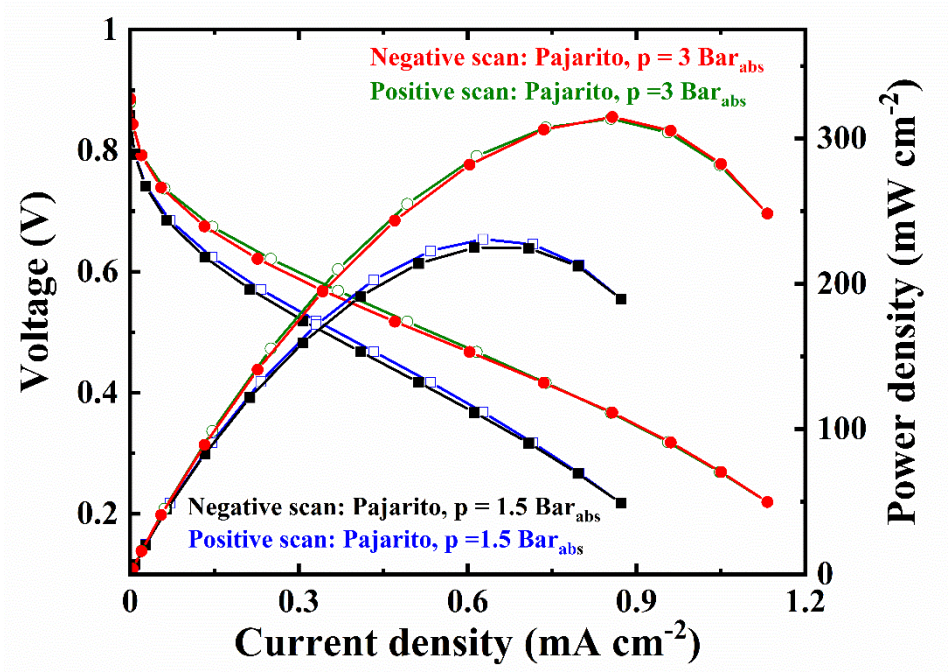

Figure SI.5 Polarization and power density curves for 25-cm² MEAs with Pajarito powder. Ink 2. Cathode catalyst loading: 2 mg cm^{-2}. Test conditions: 80 °C; H_2/air at 500/2000 mL min^{-1}, 100 % RH, and back pressure of 1.5 or 3 bar$_{abs}$.

Table SI.1 Mössbauer fitting table. Parameters derived from the fittings of Mössbauer spectra at 5 K of the: RA (%), IS ($mm \cdot s^{-1}$), QS ($mm \cdot s^{-1}$), LW ($mm \cdot s^{-1}$) and H (Tesla) of each fitted spectral component.

	Comp.	RA %	IS $mm \cdot s^{-1}$	QS $mm \cdot s^{-1}$	LW $mm \cdot s^{-1}$	H Tesla	Assignment
RFM20-800N_2-950NH_3	D1	13	0.47	1.34	0.8	-	Fe^{3+}-N_4 site
	singlet	41	0.03	-	0.97	-	γ-Fe
	Sextet 1	11	0.30	-	0.76	26	Fe_3C
	Sextet 2	35	0.66	-	1.99	44	Fe_2O_3
RFM20-800N_2-AW-950NH_3	D1	25	0.54	1.21	0.8	-	Fe^{3+}-N_4 site
	singlet	28	0.20	-	1.71	-	γ-Fe
	Sextet 2	47	0.37	-	1.77	43	Fe_2O_3

Table SI. 2 Comparison of the performance non-noble cathode catalysts for H_2/air fuel cell reported in the literatures

Catalysts	Maximum power ($mW\ cm^{-2}$)	Operating conditions (Catalyst loading, temperature, humidity, back pressure)	References
Fe-N-C aerogel	140	2 $mg\ cm^{-2}$, 80 °C, 100%, 3 bar	**This work**
Pajarito powder	315	2 $mg\ cm^{-2}$, 80 °C, 100%, 3 bar	
Fe-N-DCB	70	2 $mg\ cm^{-2}$, 80 °C, 100%, 4.5 bar	[1]
Fe/C-700	72	4.08 $mg\ cm^{-2}$, 160 °C, 100%, 1 bar	[2]
FeSAs/NPS-HC	400	0.8 $mg\ cm^{-2}$, 80 °C, 100%, 2 bar	[3]
(CM+PANI)-Fe-C	420	4 $mg\ cm^{-2}$, 80 °C, 100%, 1 bar	[4]
SiO_2-Fe/N/C	312	3 $mg\ cm^{-2}$, 80 °C, 100%, 1 bar	[5]

References:

[1] Á. García, M. Retuerto, C. Dominguez, L. Pascual, P. Ferrer, D. Gianolio, A. Serrano, P. Assmann, D.G. Sanchez, M.A. Pena, Fe doped porous triazine as efficient electrocatalysts for the oxygen reduction reaction in acid electrolyte, Applied Catalysis B: Environmental, 264 (2020) 118507. https://doi.org/10.1016/j.apcatb.2019.118507.
[2] Y. Hu, J.O. Jensen, W. Zhang, S. Martin, R. Chenitz, C. Pan, W. Xing, N.J. Bjerrum, Q. Li, Fe_3C-based oxygen reduction catalysts: synthesis, hollow spherical structures and applications in fuel cells, Journal of Materials Chemistry A, 3 (2015) 1752-1760. https://doi.org/10.1039/c4ta03986f.
[3] Y. Chen, S. Ji, S. Zhao, W. Chen, J. Dong, W.C. Cheong, R. Shen, X. Wen, L. Zheng, A.I. Rykov, S. Cai, H. Tang, Z. Zhuang, C. Chen, Q. Peng, D. Wang, Y. Li, Enhanced oxygen reduction with single-atomic-site iron catalysts for a zinc-air battery and hydrogen-air fuel cell, Nat Commun, 9 (2018) 5422. https://doi.org/10.1038/s41467-018-07850-2.
[4] H.T. Chung, D.A. Cullen, D. Higgins, B.T. Sneed, E.F. Holby, K.L. More, P. Zelenay, Direct atomic-level insight into the active sites of a high-performance PGM-free ORR catalyst, Science, 357 (2017) 479-484. https://doi.org/10.1126/science.aan2255.
[5] X. Yang, Y. Wang, G. Zhang, L. Du, L. Yang, M. Markiewicz, J.-y. Choi, R. Chenitz, S. Sun, SiO_2-Fe/N/C catalyst with enhanced mass transport in PEM fuel cells, Applied Catalysis B: Environmental, 264 (2020) 118523. https://doi.org/10.1016/j.apcatb.2019.118523.